

A Comprehensive Framework for Electroweak Phase Transitions: Thermal History and Dynamics from Bubble Nucleation to Percolation

Haibin Chen^a, Yun Jiang^{a,1}

^a*TianQin Research Center for Gravitational Physics & School of Physics and Astronomy,
Sun Yat-sen University (Zhuhai Campus), Zhuhai 519082, China*

E-mail: chenhb66@mail2.sysu.edu.cn, jiangyun5@sysu.edu.cn

ABSTRACT: The electroweak phase transition (EWPT) is crucial for cosmology and particle physics, with a profound impact on electroweak baryogenesis, symmetry breaking, and gravitational wave (GW) signals. However, many studies overlook key aspects of EWPT dynamics, leading to misidentified patterns and overestimated GW signals. To address these gaps, we present a comprehensive framework for analyzing EWPTs, focusing on the vacuum's thermal history and dynamics from bubble nucleation to percolation. Using the \mathbb{Z}_2 -odd real scalar singlet model, we demonstrate the occurrence of spontaneous \mathbb{Z}_2 symmetry breaking in the high-temperature vacuum, leading to diverse EWPT processes, including multi-step transitions and inverse symmetry breaking. We identify four distinct EWPT patterns, each characterized by unique symmetry-breaking mechanisms and associated with bubbles exhibiting distinct field configurations, which can be analyzed using a formalism based on energy density distributions developed here. A key finding is that bubble nucleation fails in extremely strong phase transitions (PTs) with low nucleation rates, or in ultra-fast PTs involving inverse s -bubbles that collapse instantly upon formation, both of which lead to false vacuum trapping and the absence of observable GW signals. In first-order PTs where nucleation succeeds, stronger transitions occur later in the universe's evolution, while weaker transitions proceed more rapidly. Multi-step transitions involving (inverse) \mathbb{Z}_2 symmetry breaking give rise to complex transition sequences and exotic bubble dynamics, such as sequential nucleation or the coexistence of bubbles from different vacua—phenomena with significant implications for GW spectra, dark matter and baryogenesis. This work advances our understanding of EWPT dynamics and lays the groundwork for future studies of EWPTs in beyond-the-Standard-Model physics.

¹Corresponding author.

Contents

1	Introduction	2
2	Effective potential description of the model	3
2.1	Zero-temperature model description	3
2.2	Finite-temperature effective potential	4
3	Vacuum phases in the thermal history	5
3.1	Symmetry breaking and high-temperature vacuum structures	5
3.2	Diverse EWPTs to the EW vacuum	6
4	Dynamics of the EWPTs	11
4.1	Four patterns of EWPTs	11
4.2	Settling into the EW vacuum at zero temperature	13
4.3	Successful bubble nucleation	14
4.4	Percolation of EWPTs	16
5	Properties of nucleated bubbles	18
5.1	Bubble profile analysis	18
5.2	Assessment of the thin-wall approximation	22
5.3	Bubble nucleation modes	23
6	Exotic bubbles in consecutive first-order PTs	25
6.1	Bubble configurations in Pattern III-1 PTs	26
6.2	Bubble configurations in Pattern IV-1 PTs	26
7	GW signals: observational signatures	28
8	Conclusions and future directions	30
	Appendices	32
A	Vacuum structure at zero temperature	32
A.1	Tree-level analysis	32
A.2	Effects of loop corrections	34
B	Field-dependent mass at finite temperature	35
C	Thermal corrections to the mass	36
D	Renormalization group equations	37
E	Surface energy density of thin-wall bubbles	38
F	Modes of bubble nucleation	39

1 Introduction

The Standard Model (SM) of particle physics, despite its remarkable success in explaining a wide range of phenomena, falls short in accounting for the observed baryon asymmetry of the universe (BAU). This discrepancy has spurred the search for new physics beyond the SM (BSM). One of the compelling solutions is electroweak baryogenesis [1–4], which dynamically generates this asymmetry during the electroweak phase transition (EWPT) in the early universe. This mechanism is particularly appealing because of its intrinsic connection to electroweak symmetry breaking (EWSB) and the potential for experimental verification at particle colliders. For a successful electroweak baryogenesis, the EWPT must be a first-order phase transition (PT) [5], which could also produce detectable gravitational wave (GW) signals [6–10]. This offers a unique opportunity to probe the EWPTs and test the underlying mechanism of EWSB.

However, lattice simulations indicate that a first-order EWPT within the SM is only possible if the Higgs boson mass is below approximately 70 GeV [11, 12]. The observed Higgs boson mass of 125.09 GeV, as measured at the Large Hadron Collider (LHC) [13], confirms that the EWPT in the SM proceeds as a smooth crossover at temperature of 159.5 ± 1.5 GeV [14, 15]. Consequently, achieving a first-order PT necessitates theoretical extensions to the SM. A broad range of BSM models, including singlet-extended models [16–26], two-Higgs doublet models (2HDMs) [27–33], supersymmetric models [34–38], and models with effective operators [39–44], have been shown to support first-order transitions within specific parameter spaces.

The study of cosmological phase transitions has evolved significantly over time. Early research primarily focused on identifying first-order EWPTs in various BSM models and evaluating the critical temperature T_c and the associated parameter $\xi_c \equiv v_c/T_c$, which quantifies the strength of the PT. It is well established that a strong first-order PT ($\xi_c > 1$) is essential for generating a sufficient baryon number asymmetry through sphaleron processes [16, 20, 21]. In recent years, however, the focus has shifted towards the study of PT dynamics, especially the onset of bubble nucleation. The nucleation temperature, T_n , at which bubble formation becomes statistically probable, is governed by the nucleation rate. This rate can be estimated semi-analytically using the thin-wall approximation [45, 46], which assumes that the size of nucleated bubbles is much larger than the thickness of their walls. While useful, the applicability of the thin-wall approximation and the theoretical uncertainties in calculating T_n remains inadequately explored. These uncertainties must be carefully controlled, as T_n plays a critical role in predicting the GW power spectrum. Furthermore, it has become clear that even when a strong first-order PT ($\xi_c > 1$) is theoretically expected, a low nucleation rate can prevent the transition from proceeding as anticipated. In such cases, the universe could remain trapped in a false vacuum state [25, 30, 37, 38, 47], potentially leading to catastrophic inflation [48, 49] and an electroweak (EW) vacuum that fails to describe the present universe. Recent numerical studies within the context of the 2HDM [30] has demonstrated that the condition for effective bubble nucleation imposes an upper limit on ξ_c , with a maximum value of approximately 1.8. This constraint sharply narrows the parameter space in which a successful first-order PT could occur and be experimentally testable at particle colliders.

Another important insight emerging from recent studies is the recognition of high-temperature vacuum phases where symmetry breaking occurs [26, 38, 50–54], challenging the long-held assumption that no symmetry was broken in the early universe. The existence of such vacuum phases prior to EWPTs introduces fascinating phenomena, including inverse symmetry breaking (ISB) [26, 38, 52, 53] and absolute symmetry non-restoration (SNR) [26, 30, 38, 52, 53]. These scenarios suggest a more intricate picture of PTs than the traditional single-step EWPT, especially in the context of multi-step PTs [32, 33, 55–58], where distinct vacuum phases emerge sequentially. Typically, multi-step transitions introduce significantly more complex dynamics, and these additional complexities demand a detailed analysis of each step, from bubble nucleation to per-

colation, to fully understand the underlying processes. In extreme cases, the interplay between successive transitions may lead to exotic bubble configurations, such as the coexistence of bubbles corresponding to different true vacuum states [59–61] or the formation of nested bubbles [57–61]. Moreover, multi-step PTs are likely to give rise to topological defects, such as domain walls, which can have a profound impact on the EWPT dynamics. For instance, domain walls may catalyze PTs by enhancing nucleation rates [62–68], or even introduce novel mechanisms that enable FOPTs by bypassing traditional bubble formation [69]. These complex phenomena greatly expand the theoretical landscape of PTs, offering profound implication for our understanding of the EWPT dynamics.

In this work, we consider an extension of the SM with a \mathbb{Z}_2 -odd real scalar singlet as a case study, aiming to establish a comprehensive framework for analyzing PTs. The simplicity and broad applicability of this model make it an ideal prototype for systematically exploring a wide range of theoretical contexts. Our primary objective is to investigate high-temperature vacuum phases in which either the EW symmetry or the \mathbb{Z}_2 symmetry is broken, and to analyze the diverse EWPT processes that emerge from these scenarios, with a particular focus on multi-step PTs. Such transitions may involve the formation of bubbles whose exterior resides in a symmetry-broken phase, or bubbles consisting of two distinct fields. To accurately characterize the properties of these bubbles, we attempt to develop a new formalism tailored to multi-field bubble configurations. Additionally, we assess the validity of the thin-wall approximation and classify the various mechanisms by which bubbles are nucleated. Through this detailed analysis, we seek to deepen our understanding of PT dynamics throughout the thermal history of the universe and identify potential observational signatures that could reveal the EWPT processes the universe may have experienced.

This paper is organized as follows. After a brief description of the model under investigation in Section 2, Section 3 analyzes symmetry breaking in the vacuum at high temperatures (above the EW scale) and summarizes the diverse EWPT processes that originate from this vacuum and occur throughout the thermal history of the universe. Section 4 focuses on the dynamics of the EWPT and bubble evolution from nucleation to percolation. Special emphasis is placed on constraints that prevent vacuum trapping and on exotic bubble configurations resulting from successive FOPTs, which are further discussed in Section 6. In Section 5, we examine the properties of nucleated bubbles, including their radius and thickness. The applicability of the thin-wall approximation is also assessed, and the nucleation mode is discussed. Section 7 explores the potential of GWs as signals to distinguish between different patterns of PTs, where EWSB occurs differently. Finally, in Section 8 we summarize the key findings of this work and offer perspectives for future research.

2 Effective potential description of the model

2.1 Zero-temperature model description

We consider the simple extension of the SM with a real scalar singlet S and impose a \mathbb{Z}_2 symmetry, under which $S \rightarrow -S$. Provided that S does not acquire a vacuum expectation value (vev), it is absolutely stable and thereby provides a possible candidate for dark matter (DM) [70, 71]. The renormalizable tree-level scalar potential is

$$V_0(H, S) = -\mu_H^2 H^\dagger H + \lambda_H (H^\dagger H)^2 + \lambda_{HS} H^\dagger H S^2 - \frac{1}{2} \mu_S^2 S^2 + \frac{1}{4} \lambda_S S^4 \quad (2.1)$$

The necessary and sufficient conditions that ensure the potential bounded from below reads

$$\lambda_H > 0, \quad \lambda_S > 0, \quad -\sqrt{\lambda_H \lambda_S} < \lambda_{HS} \quad (2.2)$$

After spontaneous breaking of the electroweak symmetry, the Higgs field H acquires a vev. We parametrize the H and S fields as follows:

$$H = \frac{1}{\sqrt{2}} \begin{pmatrix} G^+ \\ v + \hat{h} + iG^0 \end{pmatrix}, \quad S = \hat{s} \quad (2.3)$$

where $v = 246.22$ GeV corresponds to the Higgs vev at zero temperature. This parametrization gives rise to two scalar mass eigenstates (\hat{h}, \hat{s}) with squared-masses given by $m_{\hat{h}}^2 = 2\lambda_H v^2 = 2\mu_H^2$ and $m_{\hat{s}}^2 = \lambda_{HS} v^2 - \mu_S^2$, along with three massless Goldstone bosons, G^0, G^\pm , which are absorbed by the corresponding gauge bosons Z, W^\pm . The \hat{h} state is identified with the SM-like Higgs observed at the LHC, and we fix its mass at $m_h = 125$ GeV [72, 73]. To facilitate the following analysis, we trade the bare mass-squared parameter μ_S^2 for the physical mass of the singlet scalar m_S . Consequently, this model is left with three independent parameters $(m_S, \lambda_{HS}, \lambda_S)$. To escape the experimental bounds from the Higgs invisible decay, in this work we consider the mass of the singlet scalar in the range $m_S > m_h/2$ [20].

2.2 Finite-temperature effective potential

To investigate the EWPT of the model, we utilize the effective potential expressed in terms of the field condensates $h \equiv \langle h \rangle_T$ and $s \equiv \langle s \rangle_T$ at finite temperature. Schematically, the effective potential takes the form:

$$V_{\text{eff}}(h, s, T) = V_0(h, s) + V_{\text{CW}}(h, s) + V_{\text{CT}}(h, s) + V_{1\text{T}}(h, s, T) + V_{\text{daisy}}(h, s, T) \quad (2.4)$$

where the first three terms are independent of T and are given in Appendix A. In this section, we present the last two terms which are dependent on temperature T .

The term $V_{1\text{T}}(h, s, T)$ accounts for the thermal effect at one-loop level and is given by [74],

$$V_{1\text{T}}(h, s, T) = \frac{T^4}{2\pi^2} \sum_i n_i J_{B,F} \left(\frac{m_i^2(h, s)}{T^2} \right)$$

Here the summation index i runs over the contributions from the top quark, W^\pm, Z gauge bosons, as well as all Higgs bosons and Goldstone bosons. For each particle species, n_i denotes the number of degrees of freedom, and m_i is the field-dependent mass, whose explicit form is given in Appendix B. The thermal integrals $J_{B,F}$ are defined as

$$J_{B,F}(y) = \pm \int_0^\infty dx x^2 \ln \left[1 \mp \exp \left(-\sqrt{x^2 + y} \right) \right]. \quad (2.5)$$

where the upper (lower) sign corresponds to bosonic (fermionic) contributions.

The term $V_{\text{daisy}}(h, s, T)$ deals with the leading-order resummation of the ring diagrams that are introduced to fix the infra-red divergence. There are two common approaches that are used to evaluate the daisy diagrams proposed by Parwani [75] and Arnold-Espinosa [76]. For practical reason, we use the latter approach in which $V_{\text{daisy}}(h, s, T)$ is given by,

$$V_{\text{daisy}}(h, s, T) = -\frac{T}{12\pi} \sum_i n_i \left[(M_i^2(h, s, T))^{\frac{3}{2}} - (m_i^2(h, s))^{\frac{3}{2}} \right] \quad (2.6)$$

where M_i^2 are the thermal Debye masses of the bosons

$$M_i^2(h, s, T) = \text{eigenvalues}(\widehat{M}_i^2(h, s) + \Pi_i(T)) \quad (2.7)$$

Here \widehat{M}_i^2 denotes the field-dependent mass matrix, as defined in Appendix B, while $\Pi_i(T)$ encodes the thermal corrections. The explicit form of $\Pi_i(T)$ for each degree of freedom is provided in Appendix C.

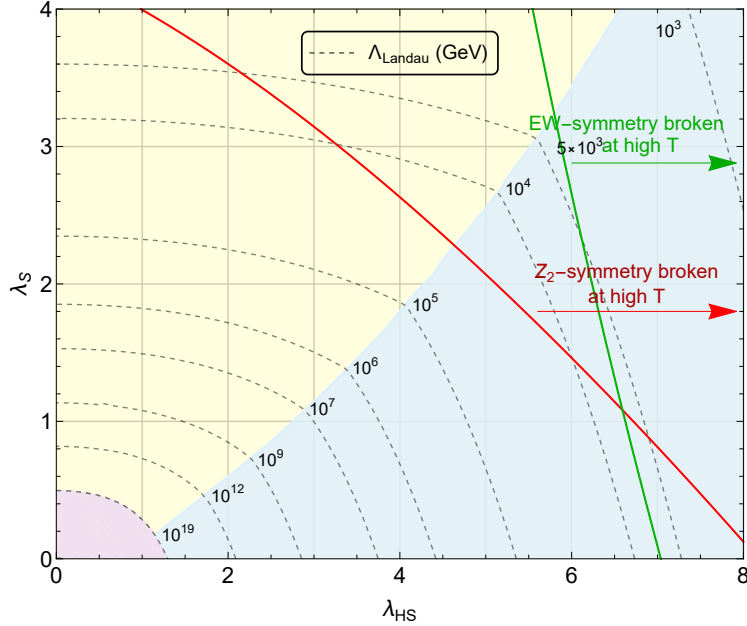


Figure 1: In the region bounded by the red and green curves, the high-temperature vacuum preserves both the EW and \mathbb{Z}_2 symmetries. Outside this region, a vacuum that breaks either EW- or \mathbb{Z}_2 symmetry emerges at sufficiently high temperatures. The dash lines indicate the mass scales above which the Landau pole arises due to the divergence or effectively exceeding the perturbative limit of λ_S (shaded in yellow) or λ_{HS} (shaded in blue). In contrast, in the purple-shaded region the Landau pole remains absent up to the Planck scale, $m_{\text{Pl}} = 10^{19}$ GeV. The renormalization group equations (RGEs) for the relevant couplings are provided in Appendix D.

3 Vacuum phases in the thermal history

3.1 Symmetry breaking and high-temperature vacuum structures

While it is commonly assumed that all the symmetries (including the EW symmetry) are preserved in the hot, early universe, it remains unclear how the EW symmetry evolves as the universe cools, or how it eventually breaks to reach a proper EW vacuum that is consistent with the measured Higgs mass at the LHC. Moreover, this assumption itself may be incorrect. By using Eq. (2.4), one can numerically trace the trajectory of the true vacuum (the global minimum of Eq. (2.4) in field space) and reconstruct the thermal history of the EW symmetry.

In fact, the assumption that the EW vacuum, when heated, resides at the origin holds only in the region bounded by the red and green curves in Fig. 1. This results from the decoupling of thermal effects, and the bound associated with the relevant couplings, λ_{HS} and λ_S , can be easily derived from the existence of a (local) minimum at the origin at very high temperature, T_{high} . Mathematically, this condition requires that the Hessian matrix at the origin

$$\mathbb{H}_{(0,0)} = \left(\begin{array}{cc} \frac{\partial^2 V_{\text{eff}}}{\partial h^2} & \frac{\partial^2 V_{\text{eff}}}{\partial h \partial s} \\ \frac{\partial^2 V_{\text{eff}}}{\partial s \partial h} & \frac{\partial^2 V_{\text{eff}}}{\partial s^2} \end{array} \right) \Bigg|_{(0,0)} \quad (3.1)$$

be positive definite at T_{high} .¹ Since the off-diagonal terms are vanishing at the origin, a sufficient

¹In general, this is a necessary but not sufficient condition, as the effective potential may have a global minimum away from the origin. However, we did not find such a scenario in this model because the contribution from the temperature-dependent terms significantly raises the effective potential in all directions around the origin.

and necessary condition for Eq. (3.1) to be positive definite is

$$\left. \frac{\partial^2 V_{\text{eff}}}{\partial h^2} \right|_{(0,0)} > 0, \quad \left. \frac{\partial^2 V_{\text{eff}}}{\partial s^2} \right|_{(0,0)} > 0. \quad (3.2)$$

Keeping the dominant T^2 term in V_{IT} and V_{daisy} components at T_{high} , we find

$$\left. \frac{\partial^2 V_{\text{eff}}}{\partial s^2} \right|_{(0,0)} \xrightarrow{\text{high } T} \frac{1}{\pi^2} (4\lambda_{HS} + 3\lambda_S) J'_B(0) - \frac{1}{4\pi} (4\lambda_{HS}\sqrt{c_h} + 3\lambda_S\sqrt{c_s}) > 0 \quad (3.3)$$

$$\begin{aligned} \left. \frac{\partial^2 V_{\text{eff}}}{\partial h^2} \right|_{(0,0)} &\xrightarrow{\text{high } T} \frac{1}{\pi^2} (12c_h - 6y_t^2) J'_B(0) + \frac{1}{\pi^2} (3y_t^2) J'_F(0) \\ &- \frac{1}{96\pi} (3\sqrt{66}g^3 + \sqrt{66}gg'^2 + 24(6\sqrt{c_h}\lambda_H + \sqrt{c_s}\lambda_{HS})) > 0 \end{aligned} \quad (3.4)$$

where $J'_{B(F)}$ denote the derivate of the bosonic (fermionic) thermal integral $J_{B(F)}(y)$ (defined in Eq. (2.5)) with respect to y and

$$c_h = \frac{1}{48} (9g^2 + 3g'^2 + 12y_t^2 + 24\lambda_H + 4\lambda_{HS}), \quad c_s = \frac{1}{12} (4\lambda_{HS} + 3\lambda_S). \quad (3.5)$$

In contrast, outside this bound, at $T \gtrsim T_{\text{high}}$, either the h -field or the s -field can develop a non-zero condensate, leading to an EW-broken or \mathbb{Z}_2 -broken vacuum. This typically happens when large couplings induce substantial thermal effect. To simplify the analysis we fix one of the couplings, i.e. $\lambda_S = 3$ as an example. As the other coupling, λ_{HS} , increases, the \mathbb{Z}_2 -broken vacuum does not appear until $\lambda_{HS} > 3.2$. However, the situation becomes complicated once $\lambda_{HS} \gtrsim 5.8$, where a new local minimum of the effective potential appears in both the h -field and s -field directions. In most cases, it is not straightforward to directly determine the vacuum phase in which the universe resided. This determination depends on which minimum has the lowest value of the effective potential, which must be numerically evaluated at T_{high} to ascertain whether the EW or \mathbb{Z}_2 symmetry was broken. The opposite situation occurs for $\lambda_S \lesssim 1$, but the \mathbb{Z}_2 -symmetry was never broken at $T \gtrsim T_{\text{high}}$. We will examine this further in Fig. 5.

3.2 Diverse EWPTs to the EW vacuum

Since we restrict the analysis to scenarios where the \mathbb{Z}_2 symmetry carried by the S field remains unbroken at $T = 0$, the EWPT must end up with an absolutely stable EW vacuum with $\langle s \rangle = 0$ (point A in Fig. 2). Possible thermal histories of the vacuum evolution are depicted in Fig. 2. Let us first consider the scenario of the EW-broken vacuum (Fig. 2(b)). In this scenario, the PTs begin from a vacuum phase with a non-zero Higgs condensate $\langle h \rangle_{T_{\text{high}}} = v' \neq 0$ (point A'), and subsequently proceed only within the $\langle s \rangle_T = 0$ plane. This implies that the \mathbb{Z}_2 symmetry remains unbroken throughout the entire process. The thermal evolution of the Higgs condensate $\langle h \rangle_T$ for different values of λ_{HS} is illustrated in Fig. 3. As the temperature T decreases, $\langle h \rangle_T$ may either jump back to the origin, resulting in an ISB

- ISB-h: $A'(v', 0) \rightarrow O(0, 0) \rightarrow A(v, 0)$

where the broken EW symmetry is restored, or it may remain non-zero due to enhanced couplings, thereby preventing a first-order PT at the EW scale

- SNR-h: $A'(v', 0) \rightarrow A(v, 0)$

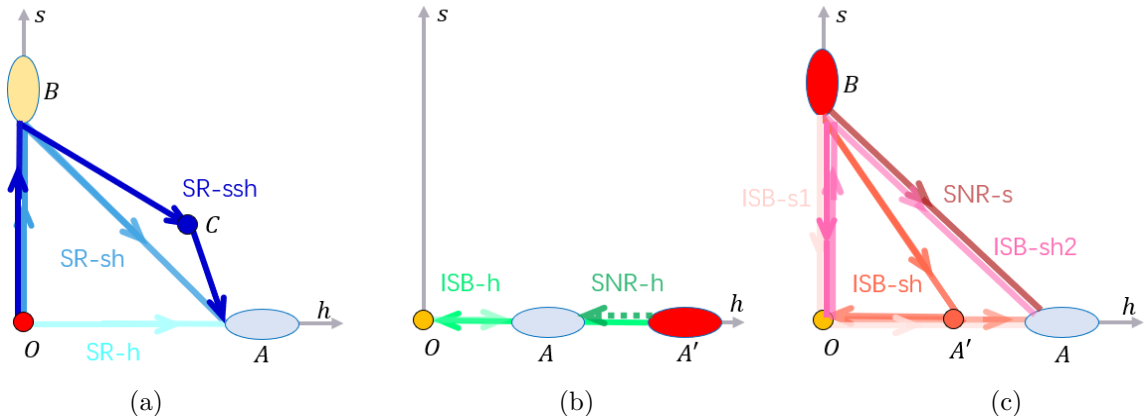


Figure 2: A schematic diagram illustrating the thermal histories of the vacuum phase, starting from three different high-temperature vacuum phases: (a) the origin, (b) an EW-broken vacuum and (c) a \mathbb{Z}_2 -broken vacuum. In each case, the arrow indicates the evolution of the vacuum as the temperature decreases.

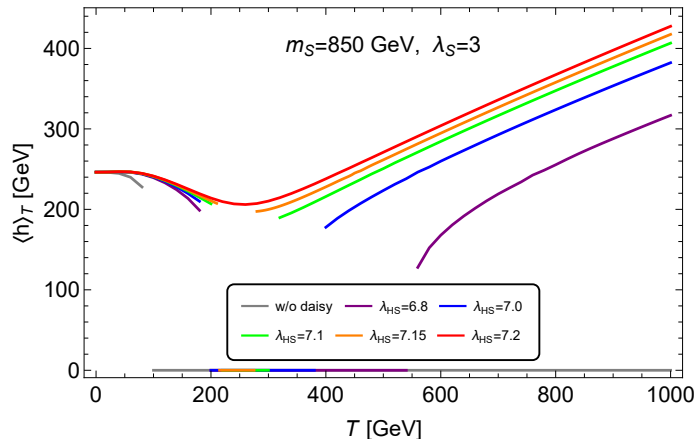


Figure 3: Phase diagrams of the EW-broken vacuum scenario are presented for different values of λ_{HS} . The SNR-h EWPT is realized for a large coupling, specifically for $\lambda_{HS} = 7.2$ (red line). In contrast, smaller values of λ_{HS} (represented by other color lines) leads to an ISB-h EWPT.

This latter scenario is called the SNR, a concept first suggested in Ref. [77] and further investigated in recent years within various BSM models [51–53, 78]. Notably, we find that SNR is closely tied to the contribution of daisy resummation. When the daisy contribution is excluded, SNR no longer occurs, as illustrated by the gray line in Fig. 3.

In the scenario of the \mathbb{Z}_2 -broken vacuum (Fig. 2(c)), prior to the EWPT, the universe resided in a vacuum where the s -field has a non-zero condensate $\langle s \rangle_{T_{\text{high}}} = w \neq 0$ (point B). Both the h and s condensates participate in the EWPT, leading to a proper EW vacuum and the restoration of the \mathbb{Z}_2 -symmetry at $T = 0$ through various possible paths. Similar to the scenario of the EW-broken vacuum, this scenario includes both one-step EWPT

- SNR-s: $B(0, w) \rightarrow A(v, 0)$

and those consisting of multiple steps, characterized by complicated thermal histories of the vacuum phase

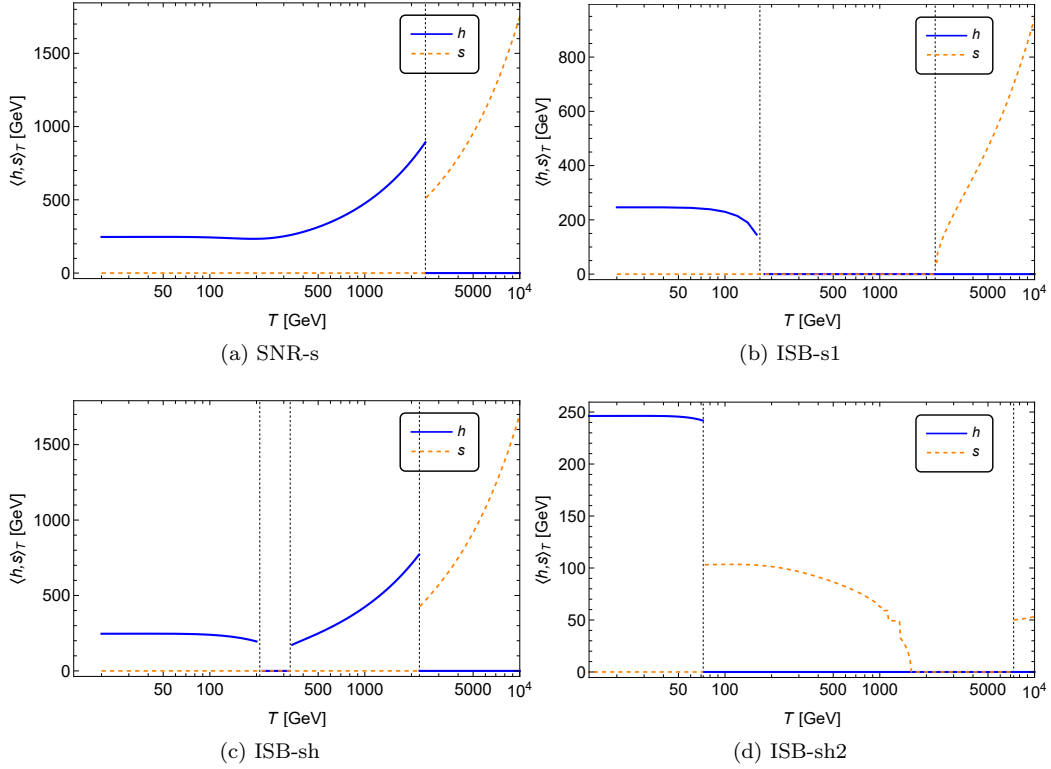


Figure 4: Possible EWPT patterns originating from the \mathbb{Z}_2 -broken vacuum scenario at $T_{\text{high}} \gtrsim 3$ TeV.

- ISB-s1: $B(0, w) \rightarrow O(0, 0) \rightarrow A(v, 0)$
- ISB-sh: $B(0, w) \rightarrow A'(v', 0) \rightarrow O(0, 0) \rightarrow A(v, 0)$
- ISB-sh2: $B(0, w) \rightarrow O(0, 0) \rightarrow B(0, w) \rightarrow A(v, 0)$.

While each of these PTs may involve potential instances of ISB, they are primarily categorized based on alternating periods of symmetry restoration and non-restoration. The phase diagrams for each EWPT pattern are shown in Fig. 4. Upon examining Fig. 4 (a), (b) and (c), we observe that at temperatures exceeding approximately 3 TeV, the s -field consistently remains in a non-zero vacuum state. As the temperature decreases, this state transitions either to point A (or A') or to point O via either a first-order or second-order EWPT. In contrast, Fig. 4 (d) reveals that a higher temperature is required for the s -field direction to manifest as a non-zero vacuum.

On the other hand, within the bound, there exists PTs starting from the vacuum phase (point O), where both the EW and \mathbb{Z}_2 symmetries were preserved at sufficiently high temperatures.

- SR-h: $O(0, 0) \rightarrow A(v, 0)$
- SR-sh: $O(0, 0) \rightarrow B(0, w) \rightarrow A(v, 0)$
- SR-ssh: $O(0, 0) \rightarrow B(0, w) \rightarrow C(v', w') \rightarrow A(v, 0)$

The SR-h EWPT is a one-step PT that proceeds only in the h -field, while the SR-sh and SR-ssh PTs involve both the h and s fields participating in the EWPT.

For the points with an absolute stable EW vacuum at zero temperature (see details in Appendix A)², we use the PhaseTracer program [79] to determine the transition pattern, the order of the transitions (for each step of multi-step PTs), and the critical temperature T_c for each first-order PT. Striking examples for three different values of λ_S are provided in Fig. 5. It is important to note that the identification of the EWPT pattern can sometimes depend on the choice of the high-temperature cutoff, T_{high} , used in the analysis. To illustrate this sensitivity in the full parameter space, we show in Fig. 5 the EWPT patterns that are possible in this model, using $T_{\text{high}} = 2$ TeV (left panel) and $T_{\text{high}} = 10$ TeV (right panel) as a comparison. Clearly, when T_{high} increases from 2 TeV to 10 TeV, a significant portion of the SR-h region transforms into the ISB-s1 pattern. For $\lambda_S = 3$, the EW-broken vacuum scenario (which includes both the SNR-h and ISB-h patterns) in the top right corner shifts to the \mathbb{Z}_2 -broken vacuum scenario, corresponding to the SNR-s and ISB-sh patterns, respectively. Additionally, the ISB-sh2 pattern appears in a small region of the SR-sh case. These changes are primarily due to the fact that as the temperature T decreases, the vacuum PTs from the \mathbb{Z}_2 -broken vacuum (phase B) to the EW-broken one (phase A) for large values of the λ_{HS} coupling, or to the origin (phase O) for relatively weak coupling. This is illustrated in Fig. 4, which shows the evolution of the vacuum phase. For example, in Fig. 4(a), if we choose $T_{\text{high}} \gtrsim 3$ TeV, the universe would have initially resided in a \mathbb{Z}_2 -broken vacuum, from which the EWPT starts, corresponding to the SNR-s pattern. In contrast, for a lower value of T_{high} (as typically considered in most analysis), an SNR-h EWPT will occur.

In general, for $\lambda_S \gtrsim 1$, the \mathbb{Z}_2 -broken vacuum scenario typically arises for moderate values of λ_{HS} , while the EW-broken vacuum scenario is only realized for extremely large values of λ_{HS} . For sufficiently high T_{high} , the value of λ_{HS} above which the \mathbb{Z}_2 -broken vacuum scenario occurs becomes independent of m_S . In fact, this value coincides with the bound derived in Eq. (3.3) (or Fig. 1) for any given value of λ_S . However, the bound that indicates the onset of the EW-broken vacuum scenario is inconsistent with the one given in Eq. (3.4). Above this bound for λ_{HS} , the effective potential in the h -field direction may possess a local minimum, but not necessarily a global one. As a result, this bound does not guarantee the emergence of a stable EW-broken vacuum. On the other hand, once $\lambda_S \lesssim 1$, the \mathbb{Z}_2 -broken vacuum phase no longer exists, regardless of the value of T_{high} . In this case, when λ_{HS} exceeds the bound in Eq. (3.4), the EW-broken vacuum phase appears at high temperatures, leading to an ISB-h EWPT.

However, it is important to note that the results regarding the SNR and ISB PTs may not be entirely reliable. This is because the analysis above is based on the one-loop effective potential at finite temperature, which is known to suffer from several theoretical issues [80]. As shown in Fig. 5, these EWPT patterns are typically generated by a large λ_{HS} , which falls within the non-perturbative regime, as discussed in other analysis [20]. Additionally, these transitions are associated with the appearance of a Landau pole Λ at a few TeVs, which raises concerns from a theoretical perspective. For instance, if the model is free from a Landau pole below 5 TeV (i.e., if $\Lambda \gtrsim 5$ TeV), then PTs starting from an EW-broken vacuum become impossible, meaning that the EW symmetry remains unbroken prior to the EWPT. Consequently, the possible PTs associated with the EWSB in this model would either begin from the origin or from a \mathbb{Z}_2 -broken vacuum, leading to the various EWPT patterns summarized in Table 1. It can be observed that the smaller the value of λ_S is, the fewer EWPT patterns are possible. Moreover, if one imposes the constraint that $\Lambda \gtrsim 10$ TeV, then only the SR-h and SR-sh are viable, provided that the three-step PTs are excluded. Furthermore, as noted in Ref. [26], models exhibiting spontaneous \mathbb{Z}_2 symmetry breaking also encompass scenarios where \mathbb{Z}_2 symmetry is not restored, even within parameter spaces characterized by small couplings. This observation suggests that the Landau pole issue is likely not

²In fact, a long-lived metastable EW vacuum remains consistent with current cosmological observations (see Sec. 4.2 for further details).

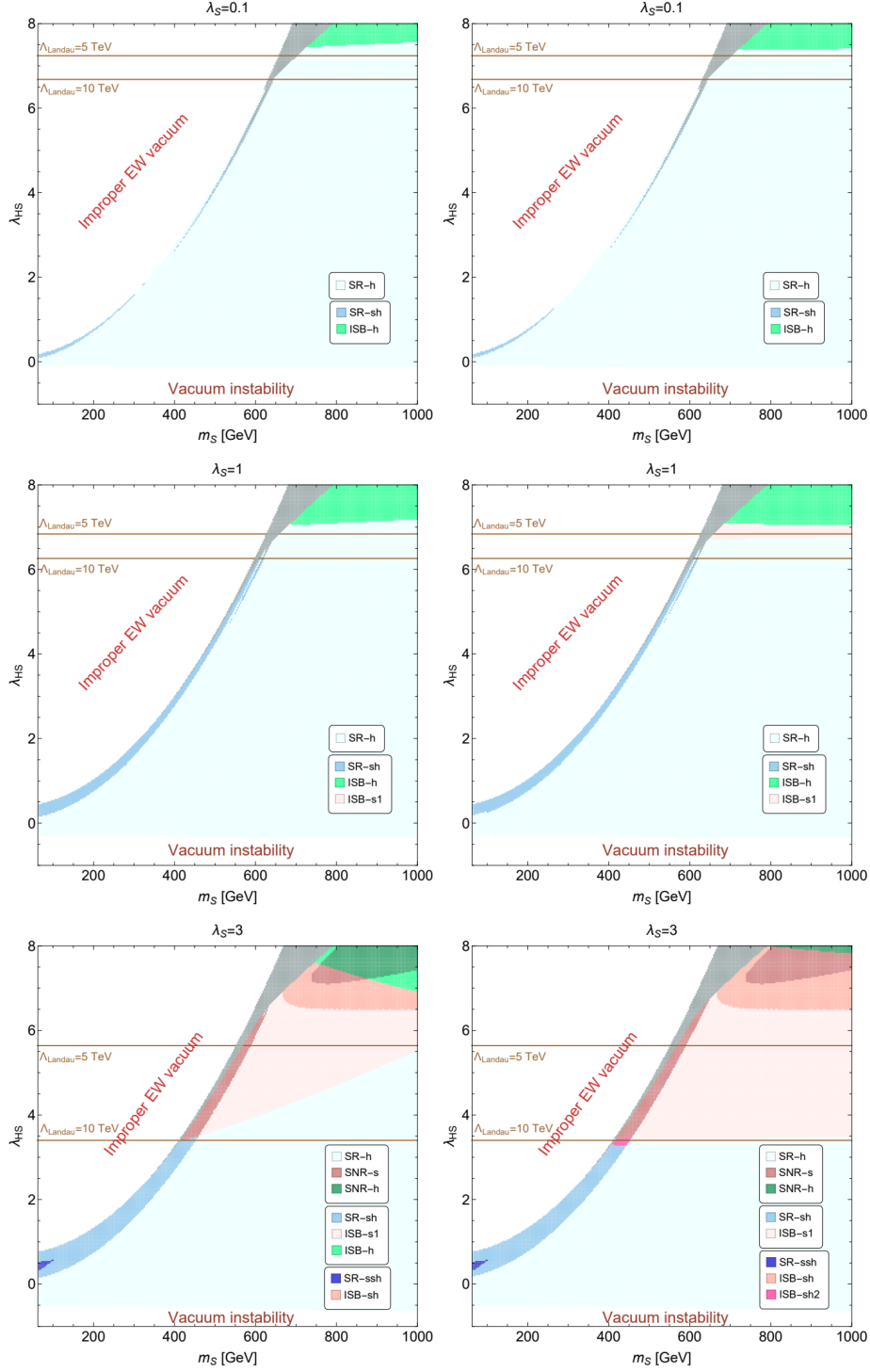


Figure 5: Possible PTs for different values of λ_S are shown. The identification of the EWPT pattern is sensitive to the choice of T_{high} , which is set to 2 TeV (left) and 10 TeV (right). An improper EW vacuum develops at $T = 0$ based on the tree-level (top-left region) and the one-loop (gray-shaded region) effective potentials. The brown lines indicate the scale of the Landau pole.

Table 1: Possible EWPT patterns are shown assuming $\Lambda \gtrsim 5$ TeV. A single tick (\checkmark) indicates the presence of the corresponding EWPT, while a double tick ($\checkmark\checkmark$) signifies that the EWPT persists even when Λ increases to $\gtrsim 10$ TeV.

Vacuum at T_{high}	EWPT patterns	Dynamics	$\lambda_S = 0.1$	$\lambda_S = 1$	$\lambda_S = 3$
The origin	SR-h (I)	one-step: $O \rightarrow A$	$\checkmark\checkmark$	$\checkmark\checkmark$	$\checkmark\checkmark$
	SR-sh (III)	two-step: $O \rightarrow B \rightarrow A$	$\checkmark\checkmark$	$\checkmark\checkmark$	$\checkmark\checkmark$
	SR-ssh	three-step: $O \rightarrow B \rightarrow C \rightarrow A$			$\checkmark\checkmark$
\mathbb{Z}_2 -broken vacuum	SNR-s (II)	one-step: $B \rightarrow A$			\checkmark
	ISB-s1 (IV)	two-step: $B \rightarrow O \rightarrow A$		\checkmark	\checkmark
	ISB-sh2	three-step: $B \rightarrow O \rightarrow B' \rightarrow A$			$\checkmark\checkmark$

Table 2: The properties related to EWPT dynamics for each phase change. P refers to unbroken symmetry, SB denotes symmetry breaking, and ISB represents inverse symmetry breaking. Note that for Pattern IV, the second step must be first-order if the first step is first-order.

Phase changes	EW	\mathbb{Z}_2	EWPT processes	First-order	T_c
$O \rightarrow A$	SB	P	I	Y/N	< 300
			IV②	Y/N	< 300
$O \rightarrow B$	P	SB	III①	Y/N	< 300
$B \rightarrow O$	P	ISB	IV①	Y/N	< 400
$B \rightarrow A$	SB	ISB	II	Y	< 300
			III②	Y	< 300

a significant concern in these cases.

4 Dynamics of the EWPTs

4.1 Four patterns of EWPTs

Among the possible EWPT patterns listed in Table 1, there are a variety of possibilities for phase changes, including SB and ISB for either symmetry. Interestingly, the same phase change can occur in different patterns of EWPT. The results are summarized in Table 2. All of these patterns consist of, at least, one step of the PT occurring at $T \lesssim v_{\text{EW}}$ during which the SB occurs with the EW symmetry. Since the SR-ssh and ISB-sh2 PTs involve three-step processes and have complex thermal history of the vacuum phase, we will not analyze them in this work. Instead, we focus on the remaining four EWPT patterns: SR-h, SNR-s, SR-sh and ISB-s1, which are denoted as Pattern I, Pattern II, Pattern III and Pattern IV, respectively. Among these, Pattern II PTs are always of first order. For Pattern III PTs, we find that the second step (III②) is always first order, while the first step (III①) can be either first or second order, denoted as Pattern III-1 and Pattern III-2, respectively. The situation for Pattern IV EWPT is more complicated. If the second step (IV②) is of second order, then the first step (IV①) must also be of second order. If IV② is first order, then IV① can be either first or second order, represented by Pattern IV-1 and Pattern IV-2, respectively. Thus, both Pattern III-1 and Pattern IV-1 consist of two first-order PTs and are marked with black dots in Fig. 6, where $T_{\text{high}} = 10$ TeV is chosen. The details of the two-step PTs will be discussed in Sec. 6.

For the case of $\lambda_S = 3$, both Pattern II and Pattern III EWPTs occur in a very narrow region of parameter space, located to the left of Pattern I and Pattern IV regions. These patterns are separated by the bound given in Eq. (3.3), which results from their different vacuum phases that

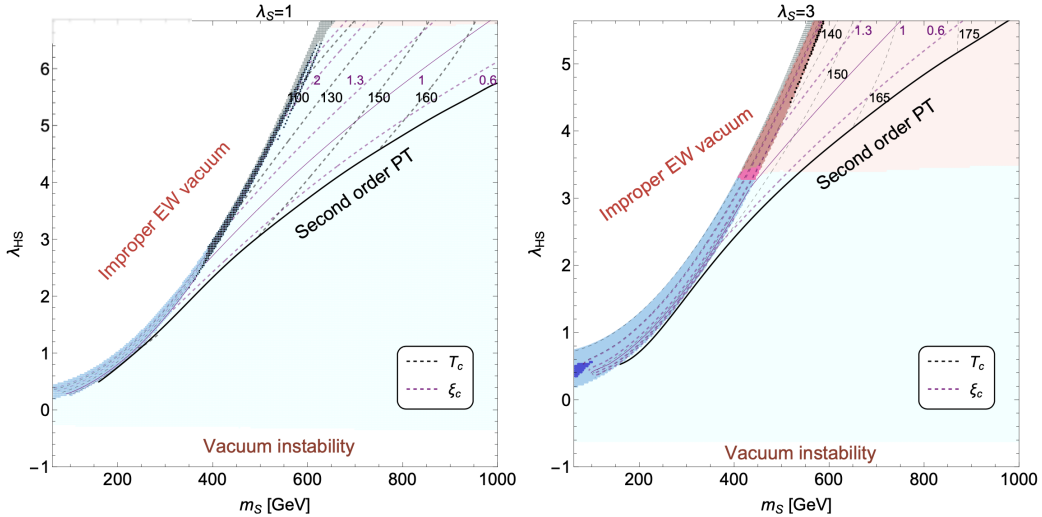


Figure 6: The same as Fig. 5. Additionally, black dots denote Pattern III-1 (left) and Pattern IV-1 (right), both of which involve two successive first-order PTs. Excluding these two EWPT Patterns, the values of T_c and ξ_c for the first-order PT in other Patterns are indicated by the black and purple contours, respectively. Below the solid curve, the EWPT is second order, and no bubbles are nucleated.

existed prior to the EWPT. Since this bound on λ_{HS} increases as λ_S decreases, Pattern II is eliminated in the small λ_S case. As expected, Pattern III-1 requires a relatively large λ_{HS} coupling and, consequently, significant thermal effects to generate a potential barrier during the first-step of the PT. However, we find that Pattern III-1 is not viable for $\lambda_S = 3$. This is because a sufficiently large λ_S induces substantial thermal effects, resulting in a \mathbb{Z}_2 -broken vacuum that instead follows Pattern II to complete the EWPT.

Excluding the two successive first-order PTs, Pattern III-1 and Pattern IV-1 (discussed in Sec. 6), Fig. 6 presents the contours of the critical temperature T_c and the PT strength $\xi_c \equiv v_c/T_c$ for the first-order PTs in the remaining Patterns. A solid purple line marks the boundary where $\xi_c = 1$, above which a ‘naive’ strong first-order PT occurs, requiring a relatively large coupling $\lambda_{HS} \gtrsim 2$. In the available parameter space, T_c ranges from 120 GeV to 180 GeV. Notably, it is possible to keep both T_c and ξ_c invariant by simultaneously decreasing the values of m_S and λ_{HS} . This is because a lower T_c in the EWPT can be achieved either by decreasing m_S or by increasing λ_{HS} , with these two opposite effects counteracting each other to maintain the invariance of T_c . In fact, each T_c contour originates from the island of the EW-broken vacuum scenario (visible in the top right corner of the $\lambda_S = 3$ case in Fig. 5), near which the dependence of T_c on m_S and λ_{HS} becomes anomalous. It is also worth noting that the contours of T_c are smoothly continuous across regions where the EWPTs proceed through different patterns.

In addition, the vacuum structure at zero temperature (see details in Appendix A) appears to play an important role in determining the pattern of the EWPT. By comparing Fig. 21 and Fig. 6, we observe that the parameter region associated with the Type C vacuum structure favors EWPTs of both Pattern I and Pattern IV (with the latter appearing only in the case of $\lambda_S = 3$). In this scenario, a PT from point O to point A is inevitable at low temperatures. This is because the Type C vacuum structure lacks stationary points of $V_0(h, s)$ in the s -field direction, forcing the transition to occur along the h -field direction. In contrast, the vacuum structures of Type A and Type B typically give rise to the EWPTs of Pattern II and Pattern III, where both the h and s fields are involved. This observation suggests that EWPTs involving both fields generally require

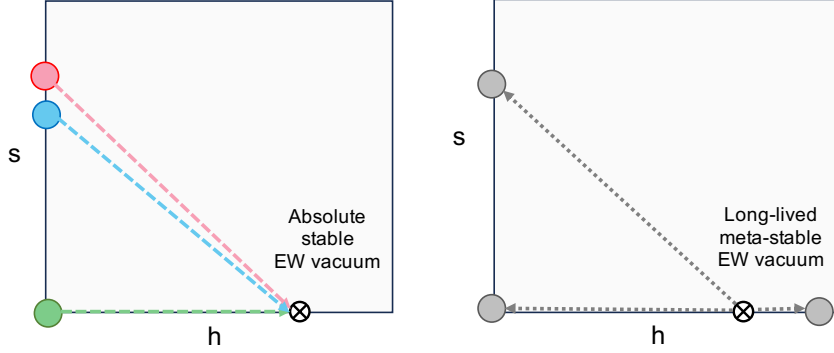


Figure 7: Two distinct thermal histories of the EW vacuum are illustrated. The black cross indicates the desired EW-broken vacuum at zero temperature. Before the EWPT, the possible vacuum phases associated with different Patterns are represented by the colored circles.

the presence of stationary points of $V_0(h, s)$ in the s -field direction, as in Type A and Type B vacua (c.f. Table 5). As the temperature increases, the stationary point characterized by $\langle s \rangle \neq 0$ evolves into a local minimum (and possibly a global minimum) of the effective potential. This process leads to the emergence of Pattern II and Pattern III. The primary distinction between these two Patterns lies in whether the breaking of \mathbb{Z}_2 symmetry occurs in the high-temperature vacuum. This outcome depends on the coupling strength and determines whether a false vacuum forms at the origin (point O) or at point B .

4.2 Settling into the EW vacuum at zero temperature

To ensure the realization of EWSB, we have so far assumed that the EW-broken vacuum is the global minimum of the zero-temperature effective potential, and the PTs from the EW-restored vacuum to it is successful. This picture of the thermal evolution is illustrated in Fig. 7 (left graph), but it may not always hold true when the full thermal history is considered. Two potentially important issues have been discussed.

First, the transition may not occur even if the EW-broken vacuum has the lowest free energy of the potential at zero temperature. In this situation, our universe would be trapped in the false vacuum that existed prior to the EWPT, which would be unable to account for EWSB and thus would be incompatible with the experimental measurements at the LHC. This phenomenon has recently been termed “vacuum trapping” [30], and its phenomenology has also been studied in the Next-to-2HDM (N2HDM) [38] and in supersymmetric models [37]. We will examine this constraint in the next section.

In contrast, another scenario is illustrated in Fig. 7 (right graph), where the EW-broken vacuum that emerges at high temperature is metastable at zero temperature. Suppose there exists a global minimum (indicated by the gray circles) with lower free energy at $T = 0$, in this case, the EW-broken vacuum could transition into this lower-energy vacuum via quantum tunneling. If the transition time exceeds the age of the universe, the metastability of the EW-broken vacuum would still be compatible with experimental results. The vacuum of Type E, as listed in Table 5, could be a candidate for realizing this possibility within the framework of this model. However, we find that in this case, the EW-broken vacuum fails to evolve into a stable vacuum throughout the thermal history, thereby ruling out this scenario within this model.

4.3 Successful bubble nucleation

Quantum tunneling to the true vacuum state proceeds through the nucleation of bubbles of the true vacuum phase within the surrounding medium of the false vacuum. The onset of nucleation critically depends on two factors: the size of the bubbles and the number of bubbles that are nucleated. Assessing these factors requires the details of the bubble profiles, denoted as $\vec{\phi}(r)$. We will postpone discussing this issue until Sec. 5.1 and will focus here on the second factor.

The nucleation rate for bubbles of the true vacuum (or the decay rate of the false vacuum) per unit time per unit volume at a finite temperature T of the Universe, denoted as $\Gamma(T)$, can be expressed in the semi-classical approximation as follows [81, 82]:

$$\Gamma(T) \approx A(T)e^{-S_E(T)} \quad (4.1)$$

where $S_E(T)$ is the Euclidean tunneling action and the dimensionful pre-factor $A(T)$ arises from the functional determinants, which are difficult to compute except in the limits, $T \ll T_{\text{dif}}$ and $T \gg T_{\text{dif}}$, where T_{dif} is the temperature corresponding to the typical size inverse R_0^{-1} of the $O(4)$ -symmetric bubble at $T = 0$ [81, 82]. In this model, we find $R_0 \simeq \mathcal{O}(10^{-1}) \text{ GeV}^{-1}$.

In both low- and high-temperature limits, the pre-factor $A(T)$ admits a simple form at leading order [81, 82],

$$A(T) \simeq \begin{cases} T_{\text{dif}}^4 \left(\frac{S_4(T)}{2\pi}\right)^2, & T \ll T_{\text{dif}} \\ T^4 \left(\frac{S_3(T)}{2\pi T}\right)^{3/2}, & T \gg T_{\text{dif}} \end{cases} \quad (4.2)$$

Here the factor T^4 is introduced for dimensional analysis. The leading contribution to $S_E(T)$ can be evaluated as follows

$$S_E(T) \simeq \begin{cases} S_4(T) = 2\pi^2 \int_0^{+\infty} r^3 dr \left[\frac{1}{2} \left(\frac{\partial \vec{\phi}}{\partial r}\right)^2 + V_{\text{eff}}(\vec{\phi}; T) \right], & T \ll T_{\text{dif}} \\ S_3(T)/T, \quad S_3(T) = 4\pi \int_0^\infty dr r^2 \left[\frac{1}{2} \left(\frac{d\vec{\phi}}{dr}\right)^2 + V_{\text{eff}}(\vec{\phi}, T) \right], & T \gg T_{\text{dif}}. \end{cases} \quad (4.3)$$

where $S_3(T)$ is often termed the three-dimensional Euclidean action.

Close to T_c the quantity S_3/T is substantially large, indicating an exponential suppression on the nucleation rate Γ . Hence, at this moment the bubbles of the true vacuum are unlikely to be nucleated. In the cosmological sense, the nucleation of bubbles becomes efficient when the first bubble is nucleated in the casual Hubble volume³

$$N(T_n) = \int_{t_c}^{t_n} dt \frac{\Gamma(t)}{H(t)^3} = \int_{T_n}^{T_c} \frac{dT}{T} \frac{\Gamma(T)}{H(T)^4} = 1 \quad (4.4)$$

Here the differential form $dT/dt = -H(T)T$ is used and T_n is defined as the nucleation temperature at which the PT begins with nucleating a handful of vacuum bubbles in the entire Hubble volume. Additionally, we relate the age of the universe to the cosmic temperature through the Hubble parameter $H(T)$,

$$H(T) = \sqrt{\frac{\rho_{\text{rad}}(T) + \rho_{\text{vac}}(T)}{3M_{\text{pl}}^2}}, \quad (4.5)$$

where $\rho_{\text{vac}}(T) \simeq V_{\text{eff}}(\vec{\phi}_F, T) - V_{\text{eff}}(\vec{\phi}_T, T)$ represents the difference in the free energy densities between the true and false vacua, and $\rho_{\text{rad}}(T) = \frac{\pi^2}{30} g_* T^4$ is the radiation energy density. In the

³Ref. [83] suggests that a first-order PT can occur without nucleating $\mathcal{O}(1)$ bubbles per unit Hubble volume. However, we leave this possibility for future work and do not consider it here.

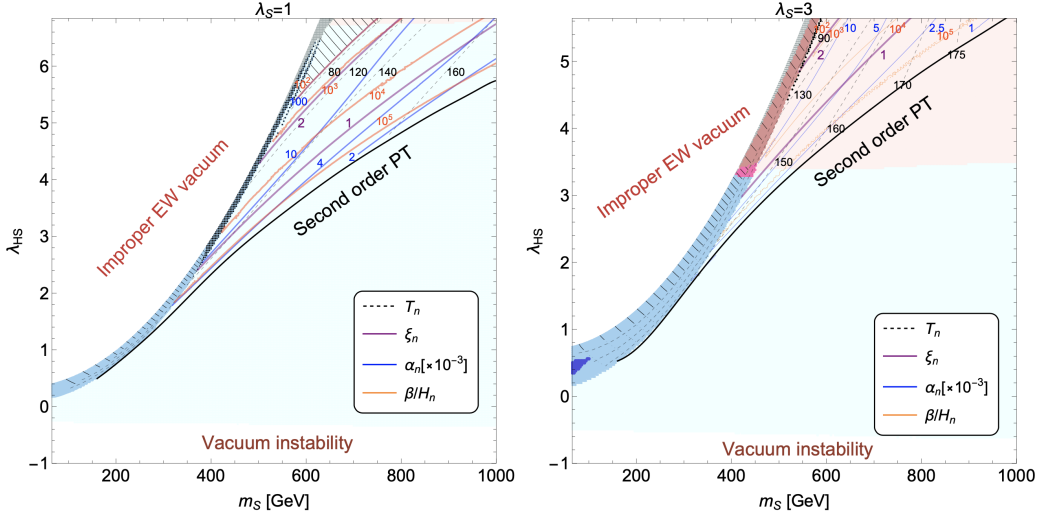


Figure 8: The same as Fig. 5. The region with backslashes indicates the failure of bubble nucleation. Contours of T_n , ξ_n , α_n , and β/H_n are also shown.

model studied here, the effective number of the relativistic degrees of freedom is $g_* \approx 106.75$. For the numerical analysis, we take the reduced Planck mass $M_{\text{pl}} = 2.4 \times 10^{18}$ GeV.

For the points that undergo first-order PTs, we evaluate the Euclidean bounce action, as given by Eq. (4.3), for temperatures $T \lesssim T_c$. The nucleation temperature T_n is then determined using the SimpleBounce [84], which employs the technique of gradient flow equations to numerically solve the bounce solution.⁴ The results are shown in Fig. 8. First of all, nucleating the bubbles of the true vacuum (in the statistical sense) is not guaranteed in any pattern of the EWPTs, even if a strong first-order PT with $\xi_c \geq 1$ is predicted. In fact, the failure (indicated by backslashes) occurs in the large λ_{HS} region, which corresponds to the largest PT strength ξ_c predicted by this model. Therefore, the constraint for successful nucleation, or the elimination of the vacuum trapping [30], places an upper bound on $\xi_c \lesssim 1.8$ independent of EWPT pattern (similar to what is observed in the two-Higgs-doublet models [30]), as well as $\xi_n \lesssim 3.2$. These constraints are independent of the EWPT patterns, whether involving single-field or double-field transitions, and regardless of whether the transition occurs in one step or two steps. This, in turns, implies that the commonly used criterion $\xi_c \gtrsim 1$ —often employed to characterize a successful strong first-order PT—is insufficient.

It might be interesting to understand what prevents the nucleation and whether this physical property is determined by the zero-temperature potential. Taking the example of the Pattern II EWPT, where hybrid h - s bubbles⁵ are nucleated, we analyze how the bounce action changes with T for different values of λ_{HS} , as illustrated in Fig. 9. Regardless of the value of λ_{HS} , the ratio S_3/T exhibits an exponential decrease near the critical temperature T_c . This occurs because that, at the onset of the PTs, the true vacuum develops a deeper minimum, and the barrier between it and the false vacuum becomes lower. Both of these effects reduce the difficulty of nucleating bubbles, leading to a significant decrease in S_3 . In contrast, at low temperatures, the barrier height

⁴Recently, a new method has been proposed to compute the tunneling action by introducing the tunneling potential [85]. While computationally fast, this method remains at the cutting edge of research for the case of multi-field PTs.

⁵The bubbles nucleated in Pattern III also consist of two fields. However, the domain walls formed in the first step can induce bubble nucleation in the vicinity of the domain wall sites, thereby making the additional contribution to the nucleation rate [62, 63]. These calculations, which involve the dynamical evolution of the DW networks, are beyond the scope of this work.

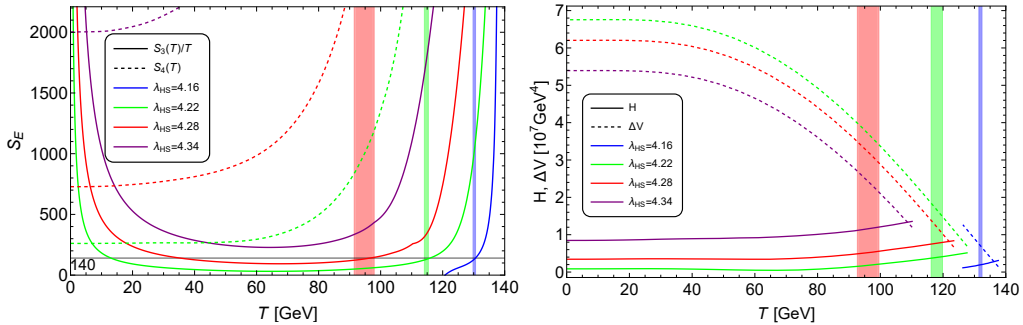


Figure 9: The action S_3/T (left) and the barrier height H and the vacuum depth of the potential ΔV (right) are shown as functions of temperature T for several examples of Pattern II EWPT with $\lambda_S = 3$ and $m_S = 500$ GeV. Each curve is computed starting from the critical temperature T_c . The shaded area represents the temperature range from the nucleation temperature T_n to the percolation temperature T_p defined in Sec. 4.4.

H and the vacuum depth of the potential ΔV become almost stable, resulting in little change in S_3 . Instead, the decreasing temperature causes S_3/T to increase. From Fig. 9, it can be observed that S_3/T decreases to a vanishingly small value just before the barrier disappears. However, for strong couplings, loop corrections become increasingly important. As a result, before S_3/T rises, it does not decrease sufficiently to the order necessary for successful bubble nucleation, leading to the absence of T_n . Consequently, the PT fails to occur, and the universe remains trapped in the false vacuum. Therefore, we conclude that regions where vacuum trapping occurs are characterized by a shallow depth between the the EW-broken vacuum and the EW-preserved vacuum in the zero-temperature effective potential. This behavior is analogous to the case of the single-field bubble, as we have verified.

In the remaining parameter regions where bubble nucleation is successful, we show the value of T_n in the dashed contours, with a solid line indicating $\xi_n \equiv v_n/T_n = 1$, above which a relatively large coupling $\lambda_{HS} \gtrsim 2$ is required. Similar to the T_c distribution, the T_n contours are also smoothly continuous, even when the EWPTs proceed with different patterns. This continuity is somewhat surprising to us for the following reasons. Determining T_n involves solving Eq. (5.1), which is non-linear, with the boundary conditions given by the false vacuum, which differs across the four Patterns. It is observed that T_n is roughly between 90 GeV and 150 GeV in both Pattern II and Pattern III(2), while the EWPTs in Pattern I and Pattern IV(2) can reach as high as 180 GeV.

4.4 Percolation of EWPTs

For successful nucleation, below T_n a growing number of bubbles emerge, expand, and collide with each other. As the bubbles continue to expand, they will absorb more regions that were initially in the old state of the metastable vacuum, and coalescence proceeds among the true vacuum bubbles.

In percolation theory, the percolation temperature T_p is defined as the temperature at which the probability of finding the false vacuum in one Hubble volume, or the volume fraction of the false vacuum, is $\mathcal{P}(T_p) = e^{-I(T_p)} \simeq 0.7^6$ [86–89]. Here, $I(T)$ represents the total volume in spheres (with appropriate multiple counting of overlaps) per unit volume of space at a given temperature

⁶The applicability of this numerical result to exotic bubble configurations, such as the co-existence of two distinct types of bubbles discussed in the next subsection, has not yet been confirmed.

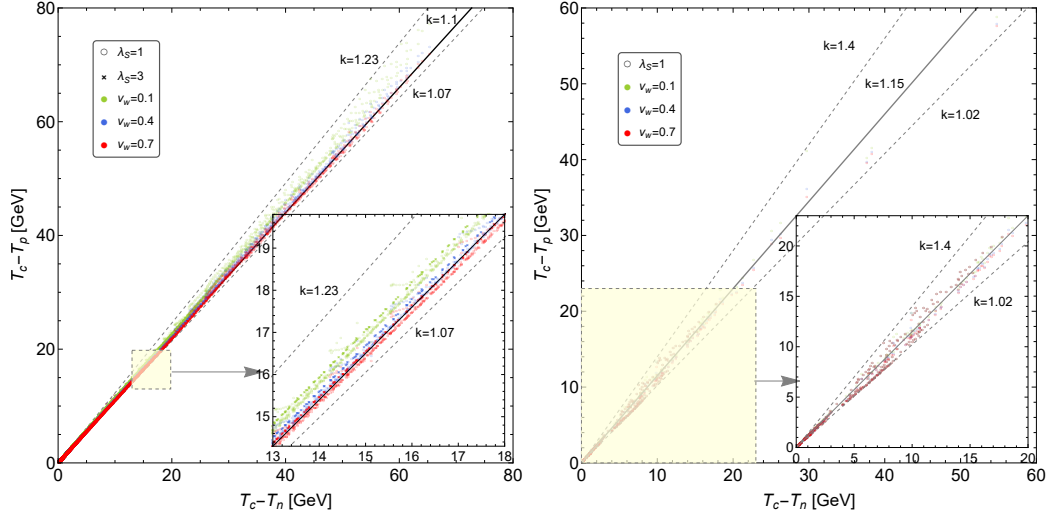


Figure 10: The numerical correlation between the differences $T_c - T_n$ and $T_c - T_p$ is shown for h bubbles from $O \rightarrow A$ transition (left) and for s bubbles from $O \rightarrow B$ transition (right). Three distinct values of the wall velocity v_w are used, each indicated by a different color. The numerical relation suggested as a useful approximation for estimating T_p is depicted by the solid line.

T [90]. The expression for it is given by:

$$I(T) = \frac{4\pi}{3} \int_T^{T_c} dT' \frac{\Gamma(T')}{H(T')T'^4} \left(\int_T^{T'} dT'' \frac{v_w(T'')}{H(T'')} \right)^3, \quad (4.6)$$

where v_w is the bubble wall velocity, which generally varies over time. Large-scale simulations [83, 86] have demonstrated that during the percolation stage, bubble collisions become highly intensive, leading to the rapid completion of the PT. Consequently, it is common to define T_p as the temperature at which the PT is effectively complete. This definition generally holds, except in the case of PTs occurring during inflation or in supercooled (or super-slow) PTs [42, 83, 91], where cosmic expansion may impede the percolation process. In such cases, it is often necessary to apply a criterion formula [42, 83, 91]

$$\frac{1}{\mathcal{V}_{\text{false}}} \frac{d\mathcal{V}_{\text{false}}}{dt} = 3H(t) - \frac{dI(t)}{dt} = H(T) \left(3 + T \frac{dI(T)}{dT} \right) < 0 \quad (4.7)$$

to determine whether the false vacuum volume begins to shrink (at least at T_p) as the temperature decreases. We numerically verified Eq. (4.7) within the parameter region where bubble nucleation is possible.

Fig. 10 demonstrates the dependence of the T_p prediction on the bubble velocity v_w and the coupling λ_S . In principle, v_w is a quantity determined by the model parameters [18, 92] but its calculation requires a high level of complexity and computational capacity, which is beyond the scope of this work. For illustrative purposes, we treat v_w as a constant parameter and select a set of values that correspond to the deflagration and detonation bubbles [93]. It turns out that the ratio $(T_c - T_p)/(T_c - T_n)$ for the phase change $O \rightarrow A$ roughly ranges from 1.07 (1.09) to 1.23 (1.15) for $\lambda_S = 1$ ($\lambda_S = 3$), while for the phase change $O \rightarrow B$, the ratio spans a broader range, from 1.02 to 1.4. A ratio greater than 1 implies that $(T_c - T_p)$ is smaller for smaller values of $(T_c - T_n)$. An extremely fast first-order PT, with highly degenerate values of T_c, T_n and T_p , is also possible and tend to occur at the highest T_c for each phase change process, as shown in Fig. 11, where $v_w = 0.8$

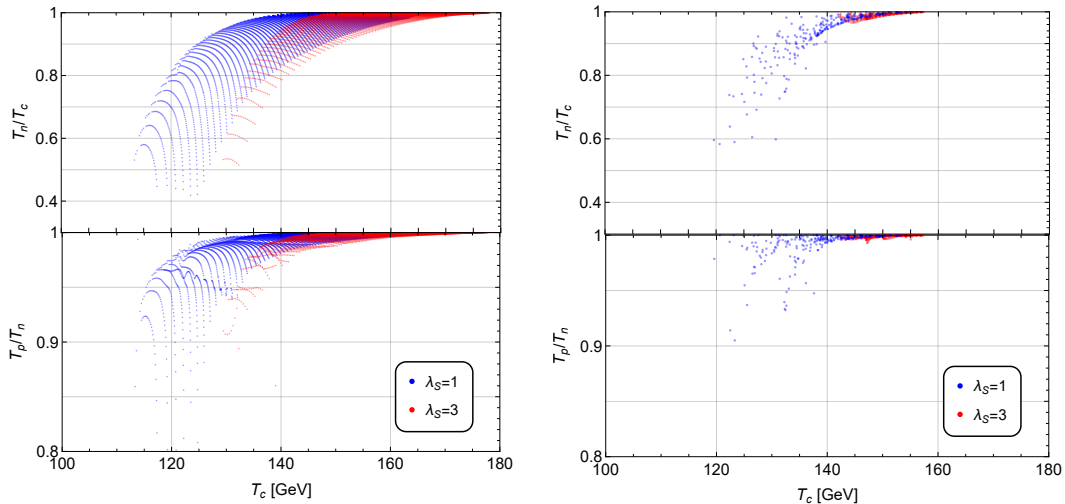


Figure 11: The plot illustrates the variations of the ratios T_n/T_c and T_p/T_n as functions of changes in T_c for the first-order PT processes, $O \rightarrow A$ (left) and $B \rightarrow A$ (right). In each case two different values of λ_S are shown for comparison, with v_w set to 0.8.

is used. For the EWPT with a lower T_c , the lower bounds of T_n/T_c and T_p/T_c exhibit a larger departure from unity, causing slower PTs with a large difference between T_n and T_p .

It can be also observed in Fig. 10 that this ratio approaches the lower bound for large v_w , which is favorable for generating large gravitational wave signals. Thus, we suggest the numerical relation $T_c - T_p = 1.1(T_c - T_n)$, which is equivalent to $T_c - T_n = 0.1(T_n - T_p)$, as a useful approximation for estimating T_p without the need for running the real-time dynamical evolution, provided that T_c and T_n are known. However, due to the lack of a rigorous derivation, it remains unclear to us whether this relation has strong model dependence.

5 Properties of nucleated bubbles

In the EWPT of all the Patterns achievable in the model, there are four distinct phase changes, which are summarized in Table 2. Generally, for each phase change involving different symmetry breaking, a specific type of bubble with a distinct field configuration can be nucleated. Since the s field condensate remains zero during the phase change $O \rightarrow A$ (which occurs in Pattern I and the second step of Pattern IV), the nucleated bubbles in these cases are constituted solely by the h field. We refer to these as the *h bubbles*. A similar situation occurs in the phase change $O \leftrightarrow B$ (which occurs in the first step of Pattern III and Pattern IV), where the h field remains zero. In these cases, the nucleated bubbles are constituted solely by the s field. We refer to the bubbles nucleated from $O \rightarrow B$ as the *s bubbles* and those from $B \rightarrow O$ as *inverse s bubbles*, due to the inverse symmetry breaking occurring in the \mathbb{Z}_2 -symmetry in the latter case. Additionally, during the phase change $B \rightarrow A$ (present in Pattern II EWPT and the second step of Pattern III), both the h and s fields participate in the PT. The nucleated bubbles in these cases are constituted by both the h and s fields, and we term these the hybrid *h-s bubbles*.

5.1 Bubble profile analysis

In any case, the vacuum bubble is characterized by two important length scales: the bubble size R_b and the bubble wall thickness L_w . These are directly associated with the wall region where

$d\vec{\phi}(r)/dr$ is large, with $\vec{\phi}(r)$ being the ‘‘bounce’’ solution of O(3)-symmetric bubbles that satisfy the classical Euclidean field equation,

$$\frac{d^2\vec{\phi}(r)}{dr^2} + \frac{2}{r} \frac{d\vec{\phi}(r)}{dr} = \vec{\nabla} V_{\text{eff}}(\vec{\phi}), \quad (5.1)$$

together with the boundary constraints

$$\left. \frac{d\vec{\phi}}{dr} \right|_{r=0} = 0, \quad \lim_{r \rightarrow \infty} \vec{\phi}(r) = \vec{\phi}_F. \quad (5.2)$$

Here the notation $\vec{\phi}$ represents the complete list of fields that make up the vacuum bubble, and $\vec{\phi}_F$ denotes the field configuration at the false vacuum. For example, $\vec{\phi} = h$ for h bubbles, $\vec{\phi} = s$ for (inverse) s bubbles, while $\vec{\phi} = \{h, s\}$ becomes two dimensional for hybrid h - s bubbles. The bounce solution can be derived either analytically or by using computational packages, especially when the form of V_{eff} is complicate or when the equations couple multiple fields. In Fig. 12 we present the four bubble profiles corresponding to each pattern. Once the bounce solution is obtained, these two scales can be determined. Numerically, R_b is defined as the r -value at which the field value reaches half of its value at the bubble center, i.e.,

$$\phi(R_b) = \frac{\phi(0) + \phi(\infty)}{2}. \quad (5.3)$$

The wall thickness L_w is given by the difference between the radii r_+ and r_- , where the bubble wall lies in the region between $r = r_-$ and $r = r_+$. For thin-wall bubbles, $r = r_{\pm}$ corresponds to the radial locations where the field value satisfies $\phi(r_{\pm}) = \phi(0) [1 \pm \tanh(1/2)]/2$ [94].

The approach described above does not work for multi-field bubbles that are nucleated in the Pattern II PTs. The reason is that there are multiple field configurations that describe the bubble, making it unclear which one should be used to determine the bubble scales. To address this issue, it will be useful to develop a formalism that identifies the typical scales of the bubble without relying on the specific bubble profile. Recall that vacuum bubbles are topological objects where the energy is strongly localized. Therefore, we suggest the bubble radius R_b can be characterized by the extremum of the energy density, i.e.,

$$\mathcal{E}(R_b) = \mathcal{E}_{\text{max}}, \quad (5.4)$$

where the energy density $\mathcal{E}(r)$ is given by

$$\mathcal{E}(r) = \frac{1}{2} (\nabla \phi_i(r))^2 + \tilde{V}(\phi(r)), \quad (5.5)$$

where $\tilde{V}(\phi(r)) \equiv V_{\text{eff}}(\vec{\phi}(r)) - V_{\text{eff}}(\vec{\phi}_F)$ is the effective potential for $\vec{\phi}(r)$, relative to the one in the false vacuum. However, there is no analogous method for determining the wall thickness L_w . Based on the observation in Fig. 12 that the distribution of the energy density resembles the Breit–Wigner shape of a resonance, we define L_w as the full width at half maximum of this distribution

$$L_w = R_2 - R_1, \quad (5.6)$$

with R_1 and R_2 being the r -values ($R_1 < R_2$) at which the energy density reaches the half sum of the peak density and the asymptotic energy density \mathcal{E}_{∞} , far from the bubble wall,

$$\mathcal{E}(R_1) = \mathcal{E}(R_2) = \frac{\mathcal{E}_{\text{max}} + \mathcal{E}_{\infty}}{2} \quad (5.7)$$

where \mathcal{E}_{∞} coincides with the difference between the free energy densities of the false and true vacuum phases, $\mathcal{E}_{\infty} = \Delta V \equiv V_{\text{eff}}(\vec{\phi}_F) - V_{\text{eff}}(\vec{\phi}_T)$.

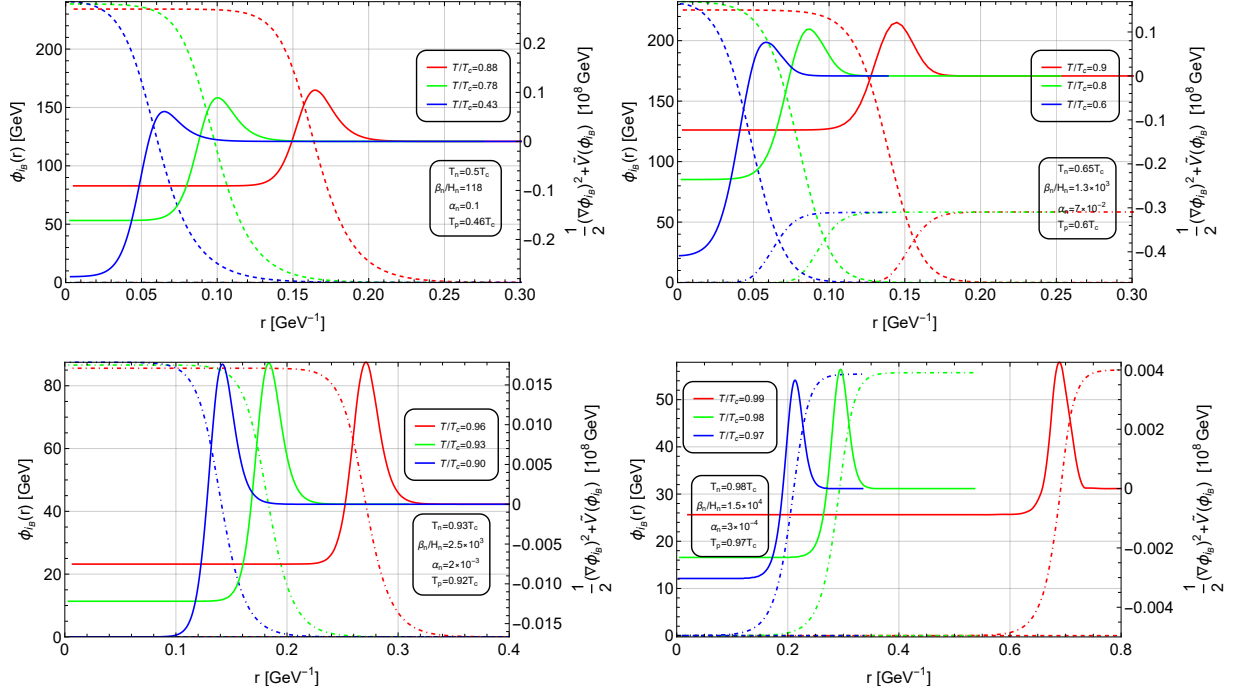


Figure 12: The bounce solution (dashed lines) and the distribution of the total energy density (solid lines) for the bubbles nucleated from the four Patterns are shown: pure h -bubble from Pattern I (top left), hybrid h - s bubble from Pattern II (top right), pure s -bubble from Pattern III (bottom left) and inverse s -bubble from Pattern IV (bottom right). The bounce solution ϕ_b use the left y-axis while the total energy density is shown in the right y-axis.

As shown in Fig. 12, for a single-field bubble, the total energy density reaches its maximum at approximately half of the field values, both inside and outside the bubble. However, for dual-field bubbles, the location of the maximum energy does not correspond to the center value of either field configuration. The comparison between two approaches for determining the bubble properties is summarized in Table 3, where we quantify the numerical error as

$$\epsilon(X) = \frac{X(\mathcal{E}) - X(\phi)}{X(\mathcal{E})}, \quad (5.8)$$

where $X(\phi)$ and $X(\mathcal{E})$ denote the quantities $X = R_b, L_w$ obtained from the bubble profiles and the energy distribution, respectively. Clearly, for single-field bubbles, the results for both R_b and L_w obtained by the two approaches are in perfect agreement at the beginning of the first-order PT during which T is close to T_c and thin-wall bubbles are typically nucleated. As T decreases, however, the results from the two approaches begin to diverge, and the difference becomes more pronounced. When the discrepancy occurs, the results based on the energy distribution predict a larger value for R_b and a smaller value for L_w . Furthermore, for a two-field bubble we observe that R_1 is close to R_b as defined in Eq. (5.3), while R_2 corresponds to the value of r at the intersection of the two field configurations, where $h(R_2) \simeq s(R_2)$. It is unclear whether this is merely a coincidence or if it suggests some deeper implication related to bubble dynamics.

Since the traditional approach based on the bubble profile is not applicable to multi-field bubbles, and the numerical errors in the two approaches for single-field bubbles is sufficiently small, we adopt the new method to analyze the bubble properties such as R_b , L_w and their ratio. The results are shown in Fig. 13. As the value of β/H from the first step of Pattern IV FOPTs exceeds

Table 3: A comparison between the traditional ϕ approach and the newly proposed \mathcal{E} approach for determining the properties of four types of bubbles such as the bubble radius R_b and the wall thickness L_w . In addition, the critical radius R_c is also included.

Bubbles	PT Patterns	T/T_c	ϕ approach		\mathcal{E} approach		Errors [%]		R_c
			$R_b(\phi)$	$L_w(\phi)$	$R_b(\mathcal{E})$	$L_w(\mathcal{E})$	$\epsilon(R_b)$	$\epsilon(L_w)$	
h -bubbles	I	0.88	0.165	0.024	0.165	0.024	0	0	0.105
	IV②	0.78	0.098	0.024	0.100	0.022	2.0	-8.3	0.047
		0.43	0.061	0.026	0.065	0.020	6.2	-23.1	0.009
h - s bubbles	II	0.90	-	-	0.144	0.024	-	-	0.141
	III②	0.80	-	-	0.086	0.020	-	-	0.079
		0.60	-	-	0.058	0.018	-	-	0.045
s bubbles	III①	0.96	0.271	0.023	0.271	0.024	0	4.3	0.213
		0.93	0.183	0.023	0.183	0.023	0	0	0.123
		0.90	0.141	0.022	0.142	0.021	0.7	-4.5	0.085
Inverse s bubbles	IV①	0.99	0.688	0.031	0.689	0.033	0.1	6.5	0.720
		0.98	0.290	0.031	0.295	0.031	1.7	0	0.279
		0.97	0.206	0.031	0.213	0.030	3.3	-3.2	0.209

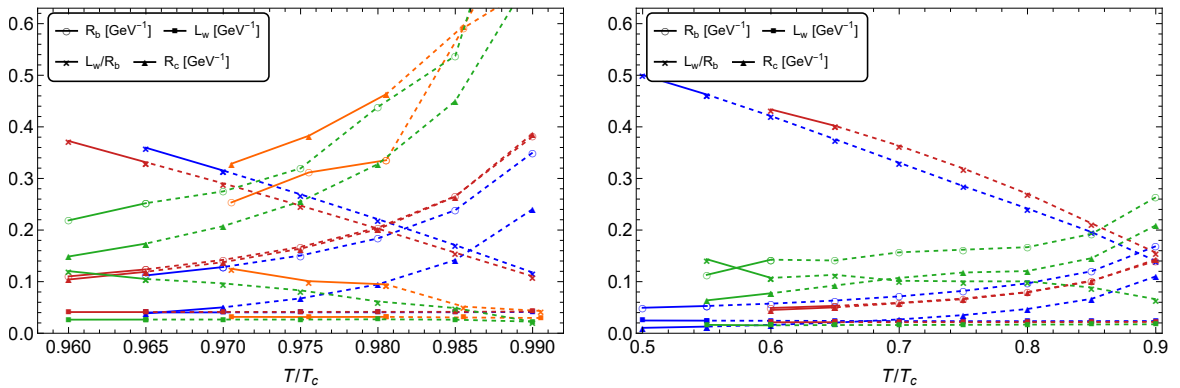


Figure 13: The evolution of bubble properties with decreasing temperature T is shown for an h -bubble (blue), a hybrid h - s bubble (red), a s -bubble (green) and an inverse s -bubble (orange) from both the fast FOPTs (left panel) and relatively slow ones (right panel). Results above T_n/T_c are depicted in dashed lines.

$\mathcal{O}(10^2)$, all inverse s -bubbles arise from ultra-fast FOPTs. For the other three types of bubble, we distinguish between those generated by fast FOPTs (left panel) and those formed by relatively slow FOPTs (right panel). For any bubble, we present results ranging from T_n/T_c to T_p/T_c . In general, bubbles formed during fast FOPTs tend to be larger than those formed during slow FOPTs. This can be understood as follows: at $r \simeq R_b$, where the bubble energy is maximized as described by Eq. (5.4), the field value reaches an inflection point, so $d^2\phi/dr^2 \simeq 0$ and $\Delta V_{\text{eff}}(\phi) \simeq 0$, effectively making $R_b^{-1}d\phi/dr$ a constant. Since $d\phi/dr$ is relatively larger for fast PTs, the bubble radius R_b is correspondingly larger. Furthermore, for bubbles nucleated at a lower T , whether from fast or slow FOPTs, the radius R_b decreases while the thickness L_w remains nearly constant. Consequently, the ratio L_w/R_b increases, reducing the accuracy of the thin-wall approximation.

Another key issue related to bubble dynamics is the determination of the critical radius R_c , below which a newly formed bubble cannot survive. To understand this, we consider a vacuum

bubble of size R , which has the free energy relative to the free energy of the false vacuum given by

$$F(R) = 4\pi R^2 \sigma - \frac{4\pi}{3} R^3 \Delta V \quad (5.9)$$

where ΔV is the difference in energy densities between the false and true vacua (as defined below Eq. (5.7)), and σ is the surface energy density of the bubble wall, which is given by:

$$\sigma = \int_0^\infty dr \frac{d\vec{\phi}}{dr} \cdot \frac{d\vec{\phi}}{dr}. \quad (5.10)$$

Here we observe that for sufficiently small sizes, the free energy of the bubble decreases as R decreases, but for sufficiently large R it changes oppositely. This implies that small nucleated bubbles will spontaneously collapse due to surface tension, whereas large bubbles will expand, causing the universe to transition to the true vacuum phase. Thus, the minimum size of a bubble that can avoid collapse is determined by the condition $dF/dR = 0$, which gives the radius of the critical bubble,

$$R_c = \frac{2\sigma}{\Delta V} \quad (5.11)$$

For single-field bubbles, σ can be obtained by solving the equation of motion while neglecting the damping term. In this case, one has

$$\frac{d\phi}{dr} = -\sqrt{2\tilde{V}(\phi)}, \quad (5.12)$$

giving rise to

$$\sigma = \int_{\phi_F}^{\phi_0} d\phi \sqrt{2\tilde{V}(\phi)}. \quad (5.13)$$

where ϕ_0 represents the field value inside the bubble, which closely approaches ϕ_T in the thin-wall limit. However, an analytical solution for two-field bubbles is not possible because, even under the thin-wall approximation, the damping terms in the coupled equations of motion cannot be simultaneously neglected due to their interdependence. The numerical result for the critical radius, R_c , for these bubbles is shown in Fig. 13 and Table 3. It is important to note that not all nucleated bubbles exceed the critical radius. An exception occurs for the inverse s -bubbles from Pattern IV $\textcircled{1}$, where the difference in vacuum energy between the interior and exterior of the nucleated bubble becomes negligible compared to the gradient energy of the bubble wall, causing the bubble to collapse due to surface tension. Additionally, for the hybrid h - s bubbles from Pattern II, the radius of the nucleated bubbles is nearly equal to critical radius.

5.2 Assessment of the thin-wall approximation

The thin-wall approximation is a crucial concept in nucleation theory, as it typically allows for semi-analytic solutions of bounce solutions or bounce actions. It is commonly employed as an initial condition in numerical simulations [45, 46]. In general, there are two popular definitions of the thin-wall approximation, which are as follows: (i) the difference in energy between the false and true vacuum, ΔV , is small compared to the height of the barrier H , and (ii) the thickness of the nucleated bubble, L_w , is much smaller than the radius, R_b . Furthermore, under the first definition, it is possible to derive a simple, approximate analytic expression for the Euclidean action S_E [95, 96],

$$S_3^{\text{TW}} = \frac{16\pi}{3} (\Delta V)^{-2} \sigma^3 \quad (5.14)$$

where σ is the surface energy density of the bubble wall, as given in Eq. (5.13).

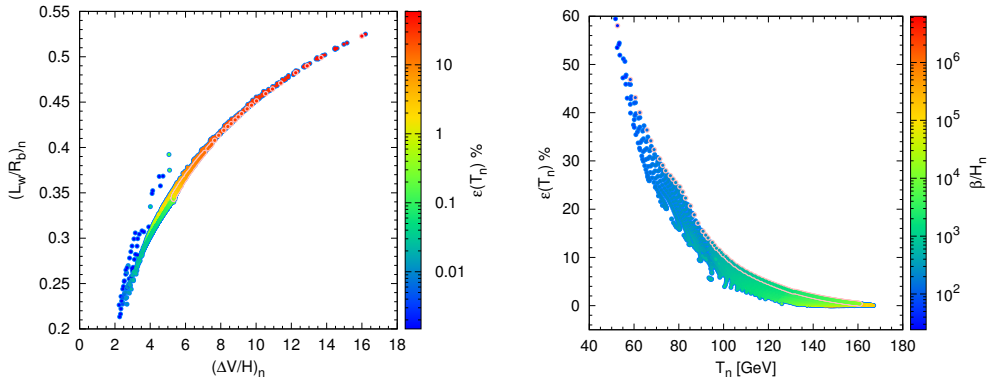


Figure 14: The applicability of the thin-wall approximation, measured by $\epsilon(T_n)$, is analyzed for the case of $\lambda_S = 1$. The left plot demonstrates the consistency of the thin-wall approximation using three different descriptions. The right plot reveals that larger values of $\epsilon(T_n)$ are associated with smaller values of β/H_n , indicating slow PTs. In both plots, points enclosed in light blue and dark blue circles correspond to Pattern I PTs and Pattern III-2 PTs, respectively, and those enclosed in pink circles represent Pattern IV PTs.

As mentioned in Ref. [97], the action obtained using the full one-loop potential may differ significantly from the one derived using the thin-wall approximation, specifically S_4^{tw} and S_3^{tw}/T [96–98]. For a quantitative assessment, we define the relative error for the action $\epsilon(S_3/T)$ and the nucleation temperature T_n , which can serve as a new way to define the thin-wall approximation:

$$\epsilon(X) = \frac{X - X^{\text{TW}}}{X} \quad (5.15)$$

where $X = S_3/T$ and T_n .

To clarify the relevance of these three definitions of the thin-wall approximation, we denote the ratio $\Delta V/H$ at a temperature of T_n as $(\Delta V/H)_n$. In the following discussion, we choose $\epsilon(T_n)$ as the quantity to assess the applicability of the thin-wall approximation, rather than using $\epsilon(S_3/T)$, based on the following considerations: T_n is a crucial physical quantity of interest in gravitational waves, and the determination of the action is aimed at obtaining the nucleation temperature T_n .

Taking the example of $\lambda_S = 1$, we examine in Fig. 14 the applicability of the thin-wall approximation, measured by $\epsilon(T_n)$. The left panel illustrates a positive correlation between $(\Delta V/H)_n$ and $(L_w/R_b)_n$, suggesting that as the ratio $(\Delta V/H)_n$ increases, the relative thickness of the bubble wall correspondingly grows. Additionally, $\epsilon(T_n)$ rises with both parameters, suggesting that $\epsilon(T_n)$, $(\Delta V/H)_n$ and $(L_w/R_b)_n$ are closely related and any of these quantities may serve as reliable indicators for assessing the validity of the thin-wall approximation. The right panel illustrates the relationship between $\epsilon(T_n)$, T_n , and β/H_n . $\epsilon(T_n)$ increases as T_n decreases, indicating that the thin-wall approximation becomes less valid at lower nucleation temperatures. Moreover, a clear relationship is observed between $\epsilon(T_n)$ and β/H_n , where lower values of β/H_n correspond to higher $\epsilon(T_n)$. This suggests that the thin-wall approximation is better suited for faster PTs with higher β/H_n . For instance, if a 10% error in $\epsilon(T_n)$ is considered acceptable, corresponding limits on the first-order PT parameters can be established: $T_n \gtrsim 100$ GeV and $\beta/H_n \gtrsim 1000$, which is approximately equivalent to $T_n - T_p \lesssim 4$ GeV.

5.3 Bubble nucleation modes

The manner in which bubbles are nucleated is of great importance in the numerical simulation of bubble collisions, as a deep understanding of how bubbles form can significantly influence simulation

outcomes. Nucleation processes during PTs can occur through various modes, each characterized by distinct features.

The modes of bubble nucleation can be classified in multiple ways based on the nature of bubble formation. Each mode provides valuable insights into how time and the underlying physical processes affect bubble formation, ultimately enhancing the accuracy of numerical simulations of bubble collisions and dynamics. As shown in Eq. (4.1), the nucleation rate Γ —the probability of nucleation events—is governed by the tunneling action $S_E(t)$. Consequently, a crucial concept in understanding these modes is the tunneling action, with each mode reflecting different behaviors as temperature declines, thereby influencing the PT dynamics.

To systematically categorize and analyze the various modes of bubble nucleation, one effective approach involves applying a Taylor expansion to the tunneling action $S_E(t)$,

$$S_E(t) = S_E(t_*) + \left. \frac{dS_E(t)}{dt} \right|_{t_*} (t - t_*) + \frac{1}{2} \left. \frac{d^2 S_E(t)}{dt^2} \right|_{t_*} (t - t_*)^2 + \dots \quad (5.16)$$

where t_* is a reference time around which the expansion is performed. The derivatives in each term are evaluated at $t = t_*$.

Three primary nucleation modes [99]—constant, exponential and simultaneous—serve as approximation approaches for $S_E(t)$, allowing the derivation of semi-analytical results.

(i) Constant nucleation: This mode is applicable when all higher-order terms in $S_E(t)$ are negligible, leaving only the zeroth-order term, which is time-independent. As a result, the nucleation rate Γ remains constant over time.

(ii) Exponential nucleation: In this mode, $S_E(t)$ is approximated using a linear expansion, corresponding to a first-order approximation. The first-order term in the expansion plays a significant role, highlighting its relevance in the nucleation process.

(iii) Simultaneous nucleation: This mode employs a Gaussian approximation that expands $S_E(t)$ to quadratic order, while the linear term contributes negligibly.

The conditions⁷ under which each mode is realized are

$$\left\{ \begin{array}{l} \frac{1}{2} \left| \frac{\beta_n}{H_n} \right| \left(\frac{T_n^2}{T_p^2} - 1 \right) \leq \epsilon_0, \text{ constant nucleation} \\ \frac{1}{2} \left| \frac{\beta_p}{H_p} \right| \left(1 - \frac{T_p^2}{T_n^2} \right) > \epsilon_0 \text{ and } \frac{1}{8} \left| \frac{3\beta_n}{H_n} + \frac{\beta_n'^2}{H_n^2} \right| \left(\frac{T_n^2}{T_p^2} - 1 \right)^2 \leq \epsilon_1, \text{ exponential nucleation} \\ \frac{1}{8} \frac{\beta_m'^2}{H_m^2} \left(1 - \frac{T_m^2}{T_n^2} \right)^2 > \epsilon_0 \text{ and } \frac{1}{16} \left| \left(\frac{5\beta_n}{H_n} + \frac{3\beta_n'^2}{H_n^2} \right) \right| \left(\frac{T_n^2}{T_m^2} - 1 \right)^3 \leq \epsilon_2, \text{ simultaneous nucleation} \end{array} \right. \quad (5.17)$$

where $\beta'^2 = H(T)^2 T^2 \frac{d^2 S}{dT^2}$ and T_m is the temperature corresponding to the time t_m at which the extremum of $S_E(t)$ occurs. The subscripts n , m and p indicate that the quantity is evaluated at the temperatures T_n , T_m and T_p , respectively. The parameters $\epsilon_0, \epsilon_1, \epsilon_2$ are the error terms introduced to assess the applicability and range of each nucleation mode.

Consider the phase change $O \rightarrow A$ as an example, in Fig. 15 we highlight the boundaries within the parameter region where different nucleation modes dominate, assuming $\epsilon_0 \sim \epsilon_1 \sim \epsilon_2 \sim 1$. Both exponential and Gaussian nucleation processes are present across the parameter region. It is evident that exponential nucleation is the predominant mode for bubble formation, indicating that, in most scenarios, the nucleation rate grows exponentially, and the formation of phase A bubbles follows an exponential probability distribution. However, a very narrow region (above the dark green curve) exists within the parameter space where Gaussian nucleation can take place. This region is located just below the boundary where the nucleation rate becomes suppressed and

⁷A rigorous derivation is provided in Appendix F.

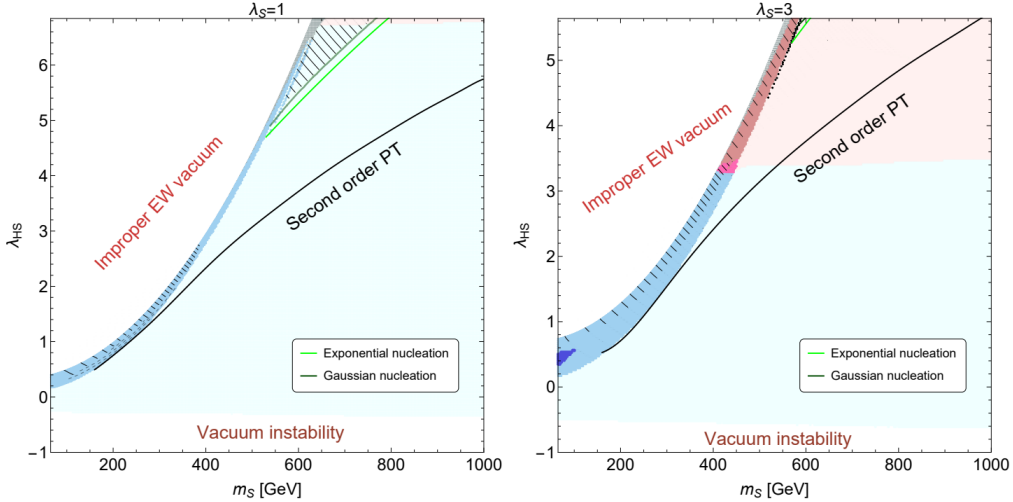


Figure 15: The distribution of nucleation modes in the parameter space for $\lambda_S = 1$ (left) and $\lambda_S = 3$ (right) is illustrated. For the $O \rightarrow A$ PT, exponential nucleation predominates, occurring in the region below the light green curve. In contrast, Gaussian nucleation happens in the very narrow region above the dark green curve.

unsuccessful bubble nucleation is resulted. This suggests that under certain conditions—likely involving a moderately suppressed rate—the formation of bubbles occurs nearly simultaneously across the system, deviating from the typical exponential behavior. While simplistic, this analysis provides valuable insights into how the bubble formation shifts with variations in the parameter space, offering a clearer understanding of the interplay between two nucleation modes commonly employed in numerical simulation.

6 Exotic bubbles in consecutive first-order PTs

In this section we present a concise analysis of two consecutive first-order PTs, specifically Pattern III-1 and Pattern IV-1. Pattern III-1 corresponds to a small value of $\lambda_S = 1$, while Pattern IV-1 occurs at a large value of $\lambda_S = 3$, as illustrated in Fig. 6. Detailed results are shown in Fig. 16. In both Patterns, we observe that the second-step transition is significantly strong, whereas the first-step transition is rather weak. As a result, bubble nucleation in the first step is always successful provided the bubbles exceed the critical size. However, nucleation in the second step is not guaranteed. In Fig. 16 we classify the points based on the occurrence of bubble nucleation in the second step. Our analysis reveals that successful nucleation in the second step is associated with a critical PT strength $\xi_{c,2} \lesssim 1.8$, consistent with the findings discussed in Sec. 4.3.

In general, the dynamics of successive FOPTs are considerably more complex. During the thermal history of Pattern III-1 (Pattern IV-1) EWPT, there exist three possible phase changes: $O(B) \rightarrow B(O)$, $B(O) \rightarrow A$ and also $O(B) \rightarrow A$ (see Fig. 2). The presence of these phase changes allows for the formation of diverse transition sequences, leading to more exotic bubble configurations in addition to the sequential formation of two-step bubbles and the vacuum trapping [25, 30, 37, 38, 47] of the intermediate $B(O)$ vacuum phase. For instance, if multiple nucleation processes occur within the same temperature range, there is a potential for the co-existence of two types of bubbles [59–61] or the emergence of nested bubbles [57–61].

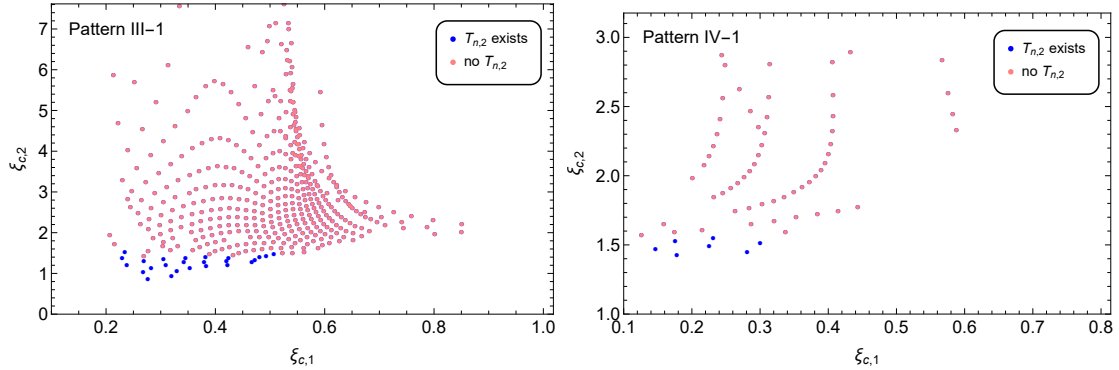


Figure 16: The PT strengths for the first and second steps, denoted by $\xi_{c,1}$ and $\xi_{c,2}$, respectively, are shown for the case of two consecutive first-order PTs: Pattern III-1 (left) and Pattern IV-1 (right). The points are categorized based on whether bubble nucleation occurs during the second step of the PT. Blue points represent successful bubble nucleation in the second step, while red points indicate failure to nucleate.

6.1 Bubble configurations in Pattern III-1 PTs

To explore the details of Pattern III-1 EWPT, we present in Fig. 17 the relevant temperature scales for all points: $T_{p,1}$ and $T_{c,2}$, which indicates the completion of the first-step PT ($O \rightarrow B$) and the onset of the second-step PT ($B \rightarrow A$), respectively. For points where bubble nucleation is successful in the second step (indicated by blue points), we find that $T_{p,1} > T_{c,2}$. This implies that the second-step PT occurs only after the first-step PT has fully completed, thereby preventing the formation of nested bubbles. In these cases, the initial O vacuum first transitions to the intermediate B vacuum through the nucleation of B bubbles, followed by a subsequent transition to the final A vacuum through the nucleation of A bubbles. Point III-1a, listed in Table 4, serves as a benchmark point for this scenario. Conversely, for points where nucleation fails in the second step, the intermediate B vacuum phase is typically trapped. Point III-1b and III-1c given in Table 4 exhibit this behavior, with the distinction being that either $T_{p,1}$ or $T_{c,2}$ is higher. However, an important exception arises when the nucleation temperature $T_n(O \rightarrow A)$ exists and $T_n(O \rightarrow A) > T_{p,1}$, corresponding to Point III-1d and highlighted by a red box in Fig. 17. In this case, as the universe cools below $T_n(O \rightarrow A)$, both A and B bubbles can nucleate within the initial O vacuum phase. This scenario represents the simultaneous occurrence of two FOPTs: $O \rightarrow B$ and $O \rightarrow A$.

6.2 Bubble configurations in Pattern IV-1 PTs

In contrast, the analysis of PT dynamics for this Pattern is less intricate. This simplicity arises because the inverse s -bubbles formed within this pattern are generally smaller than the critical bubbles, as clearly demonstrated in Fig. 13. Consequently, the transition from the B vacuum state to the O vacuum state cannot proceed via bubble nucleation, potentially leaving the universe trapped in the initial B vacuum state. Nevertheless, this description may not fully capture the PT dynamics if the potential barrier between B and O vacuum states disappears or if a direct transition from the B vacuum to the A vacuum occurs at low temperatures. Our analysis reveals that the latter scenario is impossible due to an insufficient nucleation rate, even as the free energy of the A vacuum gradually increases, causing it to become degenerate with the B vacuum before the potential barrier between B and O vanishes (as exemplified by Point IV - 1c in Table 4. Therefore, during this Pattern of EWPT, the universe first undergoes a smooth transition from the initial B vacuum to the O vacuum state when the potential barrier between B and O disappears at $T_{d,1}$. We find that $T_{d,1}$ can be either higher or lower than $T_{c,2}$, the critical temperature at which the A and

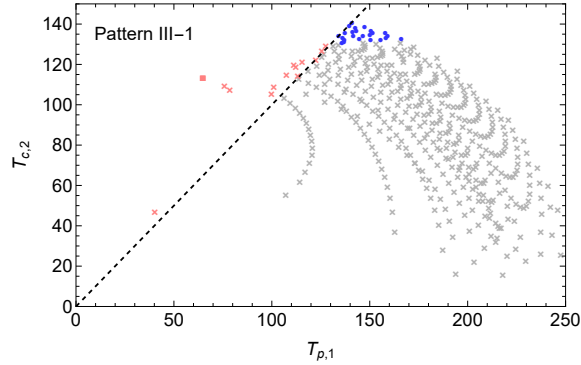


Figure 17: Temperature scales relevant to the formation of exotic bubble configurations in Pattern III-1 EWPT. Blue circles denotes successful EWPTs via sequential bubble nucleation. The red box highlights the coexistence of both A and B bubbles. In contrast, gray and red crosses indicate scenarios leading to vacuum trapping, distinguished by $T_{p,1} > T_{c,2}$ (gray crosses) or $T_{p,1} < T_{c,2}$ (red crosses).

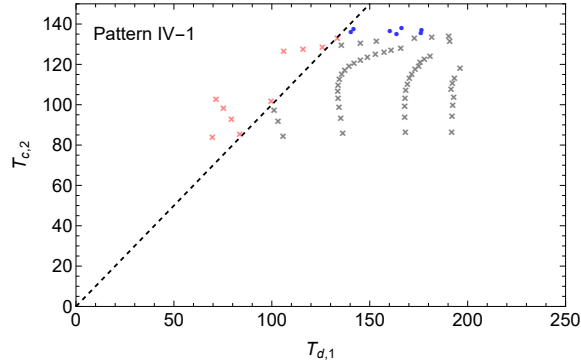


Figure 18: Temperature scales relevant to exotic bubble configurations from Pattern IV-1 EWPT. Blue circles denote successful EWPTs via bubble nucleation after a smooth first-step transition. Gray and red crosses indicate vacuum trapping, distinguished by $T_{d,1} > T_{c,2}$ (gray crosses) or $T_{d,1} < T_{c,2}$ (red crosses).

O vacuum states become degenerate while remaining separated by a potential barrier in between. This relationship is illustrated in Fig. 18. In either case, the ultimate fate of PT dynamics depends entirely on whether the second-step transition—from the O vacuum to the desired A vacuum state—can successfully occur. For cases where bubble nucleation succeeds in the second step (indicated by blue points), we find that $T_{d,1} > T_{c,2}$. This allows the universe to transition to the final A vacuum through the nucleation of A bubbles following the initial smooth transition. Point IV-1a, listed in Table 4, serves as a benchmark point for this phenomenologically viable scenario. Conversely, if the second-step transition fails, the universe remains trapped in the intermediate O vacuum, where the EW symmetry remains unbroken. These cases are represented by Point III-1b and III-1c in Table 4, differing only in the relative ordering of $T_{d,1}$ and $T_{c,2}$. Despite this difference, both cases result in the universe being confined to an EW-unbroken vacuum state, persisting until zero temperature. Such scenarios are therefore phenomenologically excluded.

Table 4: Exotic bubble configurations and their associated dynamics from the consecutive first-order PTs: Pattern III-1 (upper division) and Pattern IV-1 (lower division).

Pattern III-1 ($\lambda_S = 1$)				
Parameters	III-1a	III-1b	III-1c	III-1d
m_S	441	500	475	569
λ_{HS}	3.35	4.28	3.86	5.30
$T_c(O \rightarrow B)$	138.8	145.1	130.8	122.6
$T_n(O \rightarrow B)$	136.2	140.0	125.9	67.7
$T_p(O \rightarrow B)$	135.9	139.3	125.5	64.9
$T_c(B \rightarrow A)$	130.7	119.2	127.6	112.7
$T_n(B \rightarrow A)$	78.2	-	-	-
$T_c(O \rightarrow A)$	131.8	125.6	123.6	114.3
$T_n(O \rightarrow A)$	-	-	-	66.3
PT dynamics	$O \rightarrow B \rightarrow A$	$O \rightarrow B$ (trapped)	$O \rightarrow B$ (trapped)	$O \rightarrow B$ & $O \rightarrow A$ simultaneously
Bubble configurations	Sequential B and A bubbles in O and B vac, respectively	B bubbles only	B bubbles only	Co-existence of A and B bubbles in O vac

Pattern IV-1 ($\lambda_S = 3$)			
Parameters	IV-1a	IV-1b	IV-1c
m_S	519	556	550
λ_{HS}	4.43	5.06	4.97
$T_c(B \rightarrow O)$	167.3	174.5	143.9
$T_d(B \rightarrow O)$	166.3	172.9	133.6
$T_c(B \rightarrow A)$	-	-	134.4
$T_c(O \rightarrow A)$	138.3	133.5	133.9
$T_n(O \rightarrow A)$	131.0	-	-
PT dynamics	$B \rightarrow O \rightarrow A$	$B \rightarrow O$ (trapped)	$B \rightarrow O$ (trapped)
Bubble configurations	A bubbles in O vac	no bubbles	no bubbles

7 GW signals: observational signatures

As we understand it, the production of GWs from FOPTs begin with bubble collisions, which are typically completed by the percolation temperature T_p . Let T_* represent the temperature at which GW production occurs. In general, this gives the relation, $T_n > T_* > T_p$. For fast PTs, the approximation $T_* \simeq T_n$ is sufficiently accurate for practical purposes.

In addition to T_n , two key parameters are essential for computing the produced GW power spectrum. The first parameter quantifies the strength of the PT, defined as the ratio of the vacuum energy density to the background radiation energy density of the universe. We adopt the definition from Refs. [9, 30, 100], which is expressed as

$$\alpha_n = \frac{\rho_{\text{vac}}(T_n)}{\rho_{\text{rad}}(T_n)} = \frac{1}{\rho_{\text{rad}}(T_n)} \left(\Delta V(T) - \frac{T}{4} \frac{\partial}{\partial T} \Delta V(T) \right) \Big|_{T=T_n}, \quad (7.1)$$

where $\Delta V(T) \equiv V_{\text{eff}}(\vec{\phi}_F, T) - V_{\text{eff}}(\vec{\phi}_T, T)$, as defined in Sec. 5.1. The second parameter is the ratio β/H , which is typically expressed as

$$\beta/H_n = T \frac{d}{dT} \left(\frac{S_3}{T} \right) \Big|_{T=T_n}, \quad (7.2)$$

where the subscript n indicates that the value is evaluated at T_n . The quantity β^{-1} is related to the coefficients of the first-order terms in the Taylor expansion of the tunneling action (see Appendix F). Assuming an exponential bubble nucleation rate, β^{-1} , can be interpreted as the duration of the PT. Strictly speaking, both of these parameters should be evaluated at T_* , the temperature corresponding to the time of GW production.

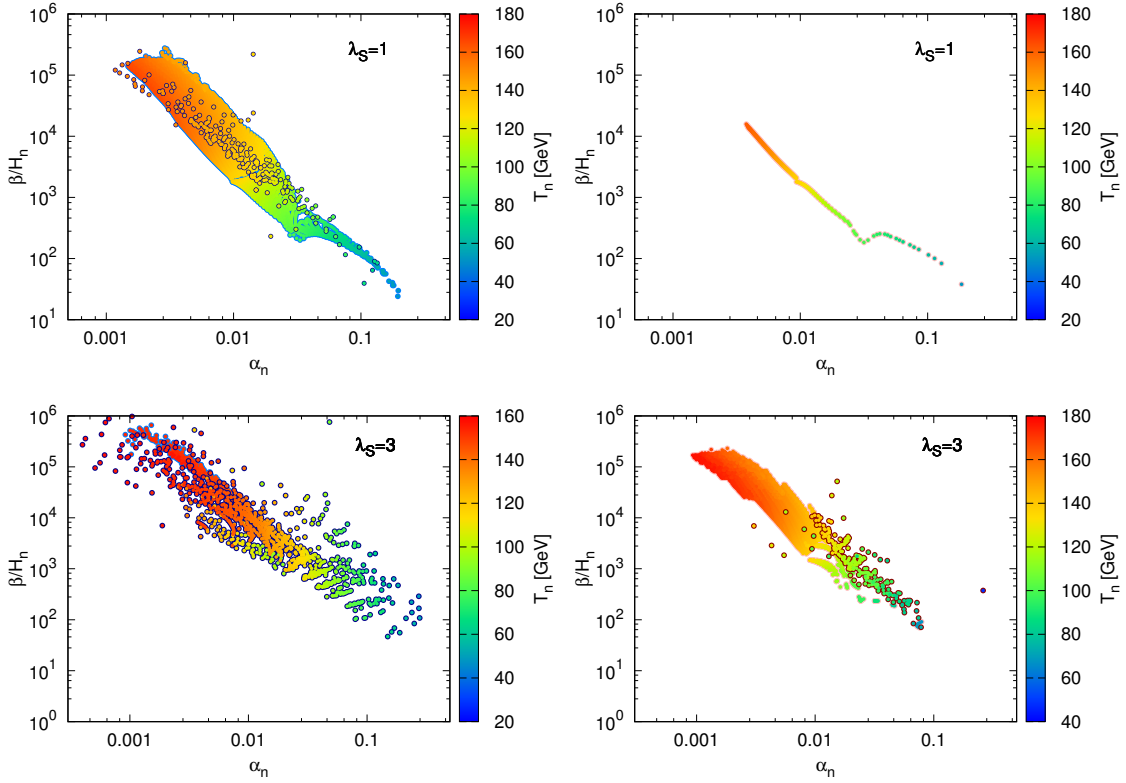


Figure 19: Key PT parameters (α_n , β/H_n , and T_n) relevant for predicting GW signals are presented in the parameter space for $\lambda_S = 1$ (upper panel) and $\lambda_S = 3$ (lower panel). For multi-step PTs (Pattern III-2 and Pattern IV-2), the parameters are evaluated for the step in which EWSB occurs. The left panel illustrate scenarios where the high-temperature vacuum resides at the origin. Like Fig. 14, points enclosed in light blue and dark blue circles correspond to Pattern I PTs and Pattern III-2 PTs, respectively. Scenarios with a \mathbb{Z}_2 -broken vacuum are depicted in the right panel, where points enclosed in dark-red and pink circles correspond to Pattern II PTs and Pattern IV-2 PTs, respectively.

Fig. 19 illustrates the strong correlation among the three key parameters that determine the production of gravitational waves. We observe that both β/H_n and T_n decrease as α_n increases. Furthermore, there is no point in the parameter space where both α_n and β/H_n take high or lower values simultaneously. This pattern reflects underlying constraints on the dynamics of the first-order EWPT. This behavior can be well understood through Fig. 8, which shows the contours of α_n and β/H_n in the parameter space that gives rise to a first-order EWPT. A key feature in these plots is that α_n and β/H_n change oppositely in magnitude as the model parameters, m_S and λ_{HS} , are varied in any direction. This inverse relationship is a direct consequence of the potential structure of the model. For instance, increasing λ_{HS} typically increases the height of the potential barrier between the two degenerate vacuum states at T_c . As the barrier height grows, the tunneling rate of the false vacuum decay is suppressed, delaying the onset of the nucleation. This delay occurs because nucleation only begins when the barrier weakens sufficiently at lower T_n . Consequently, the difference between T_c and T_n increases (which corresponds to a smaller value of β/H_n), and the deeper potential in the true vacuum generates more latent heat, thereby increasing α_n . This interplay between α_n and β/H_n leads to characteristic behaviors in EWPTs within this model.

Strong EWPTs tend to occur later in the evolution of the universe and take longer to complete. In contrast, weaker EWPTs occur earlier and can proceed with near-instantaneous nucleation in extreme cases.

Additionally, as shown in Fig. 8, the distribution of the α_n and β/H_n contours is nearly degenerate. This suggests that α_n and β/H_n are not fully independent parameters; instead, they are strongly correlated, as highlighted in Fig. 19. In this context, the typical approach where α_n , β/H_n and T_n are treated as free parameters is no longer perfectly suitable for analyzing the GW signals within this model. On the other hand, one might wonder whether it is possible to distinguish the processes through which EWSB occurred. For example, if the four Patterns discussed earlier exhibit distinctly different values for α_n , β/H_n and T_n , the resulting GW power spectrum would peak in different frequency bands, potentially. This could allow us to probe the details of the EWPT through GW detectors. To this end, we attempt to distinguish the four Patterns in Fig. 19, although the results are not as conclusive as we had anticipated. For instance, Pattern I shows the largest α_n . Most of the points, however, are similar, with the only notable difference being the lack of a specific characteristic in Pattern II.

The key difference lies in the fact that an ultra-fast EWPT, with $\beta/H_n \gtrsim 10^4$, cannot be achieved in Pattern II. This implies that Pattern II would generate a GW power spectrum that is peaked at a relatively high frequency, $f_p \gtrsim 1$ Hz, with a small amplitude—well below the sensitivity of ongoing GW detection projects like TianQin, Taiji and LISA. As a result, distinguishing Pattern II from the other Patterns will be very challenging in the near future. It remains difficult to determine whether or not the EWPTs begin with a \mathbb{Z}_2 -broken vacuum phase. However, it may not be entirely hopeless to differentiate between Pattern I and Pattern III, even though these Patterns exhibit nearly identical ranges for the relevant parameters. This is because the mechanism underlying the generation of GWs in the two-step PT process might differ significantly from those in the one-step EWPT, particularly in the presence of domain walls during the transition [62, 63, 69]. We plan to explore this issue in future work.

8 Conclusions and future directions

The study of EWPT dynamics has evolved into a sophisticated and multifaceted discipline, demanding precise modeling of the thermal history from the Big Bang to the electroweak scale, coupled with detailed analyses from bubble nucleation to percolation and the influence of topological defects. For new physics models, a comprehensive framework integrating these aspects this holistic approach is essential to uncover the full spectrum of EWPT phenomena and their cosmological implications.

In this work, we conduct an in-depth analysis of the real, \mathbb{Z}_2 -odd scalar singlet model, focusing on its thermal history and the intricate bubble dynamics during PTs. We systematically explore the vacuum structures at temperature above the TeV scale and the diverse PT processes from high-temperature vacua to the EW vacuum at low temperatures. A key finding is that spontaneous symmetry breaking can occur in the high-temperature vacuum, typically requiring large values of the couplings λ_{HS} and λ_S . However, under the constraint that the model remains free of the Landau pole below a few TeV, the scenario of an EW-broken vacuum at high temperatures is ruled out. As a result, the high-temperature vacuum prior to EWPTs either preserves symmetry or breaks the \mathbb{Z}_2 symmetry. As the universe cools, these vacua evolve to the zero-temperature EW vacuum through various pathways, including one-step, two-step, or even three-step PTs, though multi-step transitions occur only in a small region of the parameter space. Notably, the existence of a \mathbb{Z}_2 -broken vacuum phase prior to EWPTs gives rise to the unusual phenomenon of ISB.

Excluding three-step PTs, we identify four distinct patterns of EWPTs, each characterized by unique symmetry-breaking mechanisms. As a result, the bubbles nucleated in these transitions

exhibit distinct field configurations, including hybrid h - s bubbles involving both fields and inverse s bubbles arising from the ISB of \mathbb{Z}_2 symmetry. To address the complexities of analyzing these bubbles, we introduce a novel methodology based on energy-density distributions, allowing for precise determination of key properties such as bubble radius R_b and wall thickness L_w . Our analysis reveals that bubbles nucleated at lower temperatures—whether from fast or slow FOPTs—tend to have smaller radii, while their wall thickness remains nearly constant. This results in an increased L_w/R_b ratio, reducing the accuracy of the thin-wall approximation. Additionally, we find that bubbles formed during fast FOPTs are generally larger than those from slow FOPTs. However, inverse s -bubbles, which emerge from ultra-fast FOPTs associated with \mathbb{Z}_2 symmetry restoration, fail to exceed the critical radius and collapse instantaneously upon formation. This obscures the distinction between these transitions (when the potential barrier between degenerate vacua disappears) and corresponding second-order transitions. On the other hand, extremely strong FOPTs with $\xi_c \gtrsim 1.8$ in any pattern typically results in unsuccessful bubble nucleation, leading to a substantial reduction of Pattern-II EWPTs that originate from a \mathbb{Z}_2 -broken vacuum. In both cases of unsuccessful bubble nucleation, the universe may remain trapped in a false vacuum, preventing the generation of observable GW signals and making detection particularly challenging.

Conversely, for FOPTs where bubble nucleation succeeds, our analysis reveals that strong EWPTs tend to occur later in the thermal evolution of the universe and take longer to complete, whereas weaker EWPTs occur earlier and, in extreme cases, proceed with near-instantaneous nucleation. By classifying nucleation modes, we find that exponential nucleation is the dominant mechanism for bubble formation, with the nucleation rate growing exponentially in most scenarios. In contrast, Gaussian nucleation occurs only in a very narrow region of the parameter space. This classification offers key insights into how bubbles form across different patterns of PTs and provides important guidance for modeling bubble formation in numerical simulations. These advancements are crucial for refining our understanding of PT dynamics and accurately predicting the resulting GW signals.

Finally, we investigate successive FOPTs, which involve multiple phase changes occurring in sequence. These transitions demand meticulous analysis to fully unravel their dynamics and the exotic bubble configurations that emerge. By systematically assessing bubble nucleation at each PT step, we uncover complex dynamics, including sequential nucleation and the coexistence of bubbles from two distinct vacua. Such scenarios greatly increase the complexity of modeling bubble dynamics, highlighting the need for advanced theoretical frameworks and computational techniques to accurately capture and describe these intricate phenomena.

The rich EWPT processes identified in this work, particularly multi-step PTs, have profound implications for GW spectra, potentially producing distinct signals that could be detected by future GW observatories. We emphasize that the presence of high-temperature \mathbb{Z}_2 -broken vacua in Pattern II and Pattern IV prior to EWPTs leads to significant cosmological consequences and opens exciting opportunities for uncovering new physics. For instance, it may influence the relic density of dark matter, as the singlet field—when acquiring a nonzero vev in the \mathbb{Z}_2 -broken vacua—may modify its interactions with SM particles or open new annihilation channels prior to freeze-out [101–103]. Furthermore, if the singlet field interacts with the right-handed neutrinos (RHNs) N_1, N_2 , it could enhance the CP asymmetry via the decay of the heavier RHN N_2 , potentially generating a lepton asymmetry before EWPTs [103, 104]. On the other hand, spontaneous \mathbb{Z}_2 symmetry breaking in Pattern III leads to the formation of domain walls [105–107], creating regions where the EW symmetry is restored. As these domain walls propagate through space, they could generate the observed baryon asymmetry [108–111]. Both of these scenarios could provide new mechanisms for successful baryogenesis and warrant further investigation.

Overall, this study establishes a comprehensive framework for investigating complex PTs and the formation of exotic bubble configurations in a broad class of BSM models, extending well beyond the simple scalar singlet model explored here. While further validation through high-precision per-

turbative thermal field theory or non-perturbative methods is necessary, our findings provide crucial insights into the thermal history of the EW vacuum, bubble nucleation and the phenomenology of EWPTs, advancing our understanding of EWPTs in the context of BSM physics. Future studies will benefit from extending this framework through numerical simulations, exploring the interplay between PT dynamics and observable signatures, and investigating the broader implications for cosmology and particle physics.

Moreover, this work sets the stage for future investigations into multi-step PTs and their cosmological consequences, including potential GW signals and their role in shaping early-universe physics. It is also important to note that topological defects may form during multi-step PTs, significantly influencing the PT dynamics. A comprehensive exploration of these phenomena lies beyond the scope of this study but will be addressed in future studies.

Acknowledgments

We thank Tianjun Li for providing valuable suggestions regarding the Landau poles. This work is supported by the National Key Research and Development Program of China (Grant No. 2021YFC2203002) and in part by the Guangdong Major Project of Basic and Applied Basic Research (Grant No. 2019B030302001). Y. J. is also funded by the Guangzhou Basic and Applied Basic Research Foundation (No. 202102021092), the Guangdong Basic and Applied Basic Research Foundation (No. 2020A1515110150) and the Sun Yat-sen University Science Foundation.

A Vacuum structure at zero temperature

The vacuum structure defines all possible vacua (including both true and false vacua) that may coexist for a given effective potential at any temperature. This structure can vary significantly depending on the specific set of free parameters of the potential. Nonetheless, the vacuum structure can provide an important indication about the possibility of different FOPTs experienced at high temperatures. At zero temperature, the vacuum structure can be constructed by analyzing the classical values of each physical degree of freedom associated with the H and S fields. For simplicity, we neglect the irrelevant Goldstone modes and focus on the vev of two neutral fields, $\langle H^\dagger H \rangle \equiv h^2/2$ and $\langle S \rangle = s$, giving rise to the two-field potential at zero temperature,

$$V_0(h, s) = -\frac{1}{2}\mu_H^2 h^2 + \frac{1}{4}\lambda_H h^4 - \frac{1}{2}\mu_S^2 s^2 + \frac{1}{4}\lambda_S s^4 + \frac{1}{2}\lambda_{HS} h^2 s^2 \quad (\text{A.1})$$

The values of h and s at the potential minimum correspond to the homogenous background of the H and S fields. Therefore, constructing the vacuum structure involves finding the minima of the potential, Eq. (A.1).

A.1 Tree-level analysis

The minima of the tree-level potential are determined by the minimization conditions,

$$\begin{cases} \frac{\partial V_0}{\partial h} = h(\lambda_H h^2 + \lambda_{HS} s^2 - \mu_H^2) = 0, \\ \frac{\partial V_0}{\partial s} = s(\lambda_{HS} h^2 + \lambda_S s^2 - \mu_S^2) = 0. \end{cases} \quad (\text{A.2})$$

Mathematically, Eq (A.2) has 9 possible stationary points, which could be either local extrema or saddle points. However, some of these points may be eliminated depending on the specific set of model parameters. Due to the symmetric structure of the potential in the $h-s$ field space, as given by Eq. (A.1), it is sufficient to focus on the four stationary points: one at the origin $(0, 0)$, two along the direction of the either field, $(v, 0)$ and $(0, w)$, and one in the first quadrant, (v_h, w_s) . Based on

Table 5: The table summarizes the four potential stationary points in the tree-level potential at zero temperature: $(v, 0)$, $(0, 0)$, $(0, w)$ and (v_h, w_s) , where $v = \pm\mu_H/\sqrt{\lambda_H}$, $w = \pm\mu_S/\sqrt{\lambda_S}$. $v_h \neq v$ and $w_s \neq w$ are the non-trivial solutions determined by the minimization conditions, Eq. (A.2). A \checkmark indicates a stationary point, while $—$ indicates that the point is stationary. The last four cases are excluded because $(v, 0)$ is not a stationary point, precluding the possibility of EW vacuum. For the remaining cases, the properties of the stationary points are analyzed with the following possibilities: GMin: Global minimum, LMin: Local minimum, LMax: Local maximum, Sad: Saddle point. Neither Type D nor Type E can support a stable EW-broken vacuum, rendering them phenomenologically infeasible.

Type	Potentially stationary points				Status
	$(v, 0)$	$(0, 0)$	$(0, w)$	(v_h, w_s)	
A	\checkmark GMin	\checkmark LMax	\checkmark LMin	\checkmark Sad	Viable
B	\checkmark GMin	\checkmark LMax	\checkmark Sad	$—$	Viable
C	\checkmark GMin	\checkmark Sad	$—$	$—$	Viable
D	\checkmark LMin	\checkmark Sad	$—$	\checkmark Sad	No stable EW vacuum
E	\checkmark LMin	\checkmark LMax	\checkmark GMin	\checkmark Sad	Improper EW vacuum
F	$—$	\checkmark	\checkmark	\checkmark	Excluded
G	$—$	\checkmark	\checkmark	$—$	Excluded
H	$—$	\checkmark	$—$	\checkmark	Excluded
I	$—$	\checkmark	$—$	$—$	Excluded

the properties of these four points, we categorize the 9 different cases in Table 5. Among these, we exclude the last four cases where the stationary point at $(v, 0)$ is not possible, thus preventing a proper electroweak (EW) symmetry breaking. Furthermore, Type D and Type E are physically unreasonable because the point $(v, 0)$ is not the global minimum of the potential and, therefore, cannot serve as the stable EW vacuum. As a result, only three cases remain, under the requirement that $(v, 0)$ is the global minimum.

For the remaining Types (A, B, C), we analyze the property of the possible stationary points, as these will influence the dynamics of EWPT, as discussed in Sec 4.1. The contours of V_0 , Eq. (A.1), for these cases are shown in Fig. 20. In Type C, the potential along the s -axis has a stationary point at the origin $(0, 0)$, which is a saddle point. The situation is more intricate in Type A and Type B. In these cases, the origin $(0, 0)$ can be either a local maximum or a saddle point. The key difference lies in the behavior of the point $(0, w)$: in Type A, it is a local minimum, whereas in Type B, it is a saddle point. This distinction has significant implications for the PT dynamics.

In Fig. 21 we show the three possible vacuum structures in the parameters space (m_S, λ_{HS}) for three different values of $\lambda_S = 0.1, 1, 3$. Once λ_S is fixed, the requirement for vacuum stability produces a lower bound on λ_{HS} . This bound is independent of the scalar mass m_S and decreases slightly with increasing portal coupling λ_S , thereby expanding the parameter space that allows for a proper and stable EW vacuum. For any value of m_S above this lower bound, the potential always has a stable global minimum. As the coupling λ_{HS} increases, the potential along the s -direction generates a barrier, and the vacuum structure transitions from Type C to Type B. If λ_{HS} is sufficiently large, this barrier curls and forms a local minimum, leading to Type A vacuum structure. However, λ_{HS} cannot be arbitrarily large, or else the potential at the point $(v, 0)$ will be lifted above the other minima, resulting in an improper EW vacuum. This sets an upper bound on λ_{HS} , which increases with m_S . On the other hand, for a small value of λ_S , it becomes difficult to realize Type A and Type B vacuum structures. This is because the existence of Type B (and Type A) vacuum structure demands the minimum value condition for vacuum: $(\lambda_{HS}v^2 - m_S^2)^2 < \lambda_S\mu_H^4/\lambda_H$.

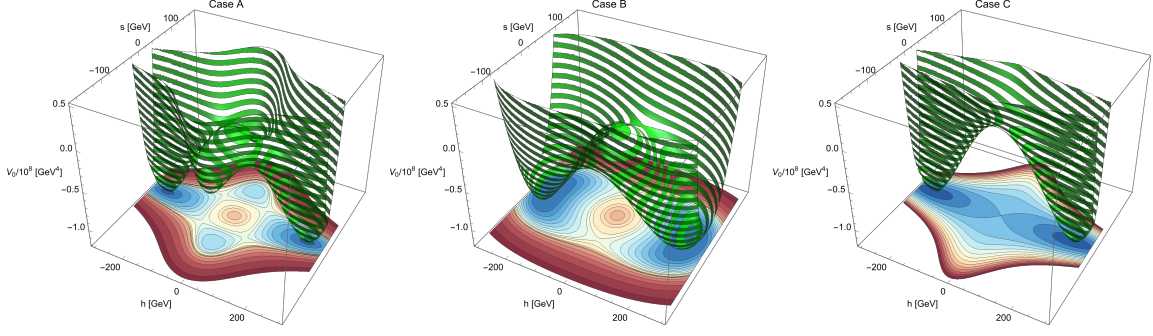


Figure 20: The three-dimensional contours and the two-dimensional projections of the tree-level potential, Eq. (A.1), for scenarios where the vacua of Type A, B, and C (from left to right) are established at zero temperature. The horizontal axes represent the h and s field directions, while the vertical axis shows the value of $V_0/10^8$.

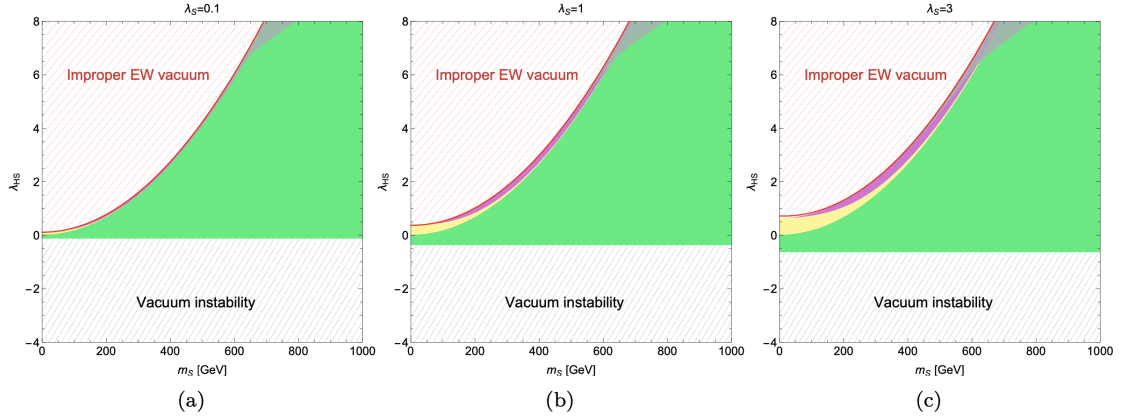


Figure 21: The vacuum structures across the parameter space are illustrated for different values of λ_S : (a) $\lambda_S = 0.1$, (b) $\lambda_S = 1$, and (c) $\lambda_S = 3$. The grey-hatched region at the bottom corresponds to Type D vacuum, where the EW vacuum is unstable. An improper EW vacuum, classified as Type E, is generated at tree level (red-hatched) and at one-loop level (gray-shaded). These cases fail to produce a stable EW vacuum at zero temperature and are therefore excluded. The remaining parameter space supports a proper and stable EW vacuum with the following vacuum structures: Type A (represented by the purple-shaded region), Type B (by the yellow-shaded region) and Type C (by the green-shaded region).

As λ_S decreases, the relationship between λ_{HS} and m_S^2 approaches a straight line. In other words, this region converges towards a parabolic curve in the $m_S - \lambda_{HS}$ plane.

A.2 Effects of loop corrections

In addition to tree-level term given in (A.1), the vacuum structure of the model is also influenced by loop corrections to the effective potential. The one-loop corrections, commonly known as the Coleman-Weinberg potential [112], provide the dominant contribution. In the $\overline{\text{MS}}$ renormalization scheme, it takes the form

$$V_{\text{CW}}(h, s) = \frac{1}{64\pi^2} \sum_i (-1)^{2s_i} n_i m_i^4(h, s) \left[\ln \frac{m_i^2(h, s)}{Q^2} - C_i \right] \quad (\text{A.3})$$

The sum over i includes contributions from the top quark, W^\pm , Z^0 bosons, all Higgs bosons and Goldstone bosons. In the sum, s_i and n_i denote the spin and the numbers of degree of freedom for the i -th particle. The field-dependent squared masses $m_i^2(h, s)$ are functions of the two fields h and s , and can be derived from the mass matrix as outlined in Appendix B. The renormalization scale Q is fixed at $Q = v$. In the $\overline{\text{MS}}$ scheme used, $C_i = 5/6$ for gauge bosons and $C_i = 3/2$ for fermions and scalar bosons.

With the inclusion of V_{CW} , the EW vacuum $(v, 0)$ at zero temperature is typically shifted. Consequently, a correction to the Higgs boson mass arises beyond the tree-level value m_h^2 , which is given in Sec. 2.1 and fixed at 125 GeV. To counteract this shift, a so-called ‘‘counter-term’’ (CT) can be manually introduced, provided that the following relations are satisfied at the EW vacuum,

$$\left. \frac{\partial V_{\text{CW}}}{\partial h} \right|_{(v,0)} = - \left. \frac{\partial V_{\text{CT}}}{\partial h} \right|_{(v,0)}, \quad \left. \frac{\partial^2 V_{\text{CW}}}{\partial h^2} \right|_{(v,0)} = - \left. \frac{\partial^2 V_{\text{CT}}}{\partial h^2} \right|_{(v,0)}, \quad \left. \frac{\partial^2 V_{\text{CW}}}{\partial s^2} \right|_{(v,0)} = - \left. \frac{\partial^2 V_{\text{CT}}}{\partial s^2} \right|_{(v,0)}. \quad (\text{A.4})$$

Respecting the invariance of gauge symmetry, the general form of the CT is parametrized as

$$V_{\text{CT}}(h, s) = \frac{1}{2} \delta\mu_H^2 h^2 + \frac{1}{4} \delta\lambda_H h^4 + \frac{1}{2} \delta\mu_S^2 s^2 + \frac{1}{4} \delta\lambda_S s^4 + \frac{\delta\lambda_{HS}}{2} h^2 s^2 \quad (\text{A.5})$$

with 5 free coefficients to be determined. First, $\delta\mu_H^2$ and $\delta\lambda_H$ can be directly evaluated from the first two conditions in Eq. (A.4). The remaining coefficients are determined by requiring the cancellation of shifts at other stationary points.

For example, in Type A and Type B vacuum structures, the point $(0, w)$ is a local minimum and a saddle point, respectively. The coefficients $\delta\mu_S^2$ and $\delta\lambda_S$ can be simultaneously determined by applying the following conditions at this point

$$\left. \frac{\partial V_{\text{CW}}}{\partial s} \right|_{(0,w)} = - \left. \frac{\partial V_{\text{CT}}}{\partial s} \right|_{(0,w)}, \quad \left. \frac{\partial^2 V_{\text{CW}}}{\partial s^2} \right|_{(0,w)} = - \left. \frac{\partial^2 V_{\text{CT}}}{\partial s^2} \right|_{(0,w)}. \quad (\text{A.6})$$

In contrast, in Type C vacuum structure, the point $(0, w)$ is not stationary, leaving $\delta\lambda_S$ unconstrained. In our analysis, we set $\delta\lambda_S = 0$ and determine $\delta\mu_S^2$ by imposing the condition at the origin $(0, 0)$

$$\left. \frac{\partial^2 V_{\text{CW}}}{\partial s^2} \right|_{(0,0)} = - \left. \frac{\partial^2 V_{\text{CT}}}{\partial s^2} \right|_{(0,0)}. \quad (\text{A.7})$$

Once $\delta\mu_S^2$ is determined, $\delta\lambda_{HS}$ can be derived from the last condition of Eq. (A.4), completing the full solution for the CT term. It is worth noting that the construction of the CT is not unique.⁸

While the constructed CT fully cancels the vacuum shift, it may fail to generate a sufficiently large potential to counteract the effect of V_{CW} at the EW vacuum. If V_{CW} raises the potential at the EW vacuum above that of other local minima, and the CT does not adequately lower the lifted potential, the proper EW vacuum established at tree level will be destabilized by loop corrections. As illustrated in Fig. 21, this destabilization effect becomes increasingly significant for larger values of λ_S .

B Field-dependent mass at finite temperature

In this model, the masses of the scalar fields H and S are field-dependent, meaning their effective masses depend on the values of h and s at the potential minima. The field-dependent nature of the mass terms arises because the background values of the fields modify the potential, which in turn affects the mass terms.

⁸For example, one of the conditions in Eq. (A.6) can be replaced by $\left. \frac{\partial^2 V_{\text{CW}}}{\partial h^2} \right|_{(0,w)} = - \left. \frac{\partial^2 V_{\text{CT}}}{\partial h^2} \right|_{(0,w)}$. We have verified that this alternative approach excludes a larger parameter space due to the requirement of a proper EW vacuum at zero temperature.

The corresponding squared-mass matrix for the fields h and s is given by:

$$\widehat{M}_{h,s}^2 = \begin{pmatrix} \frac{\partial^2 V_0}{\partial h^2} & \frac{\partial^2 V_0}{\partial h \partial s} \\ \frac{\partial^2 V_0}{\partial h \partial s} & \frac{\partial^2 V_0}{\partial s^2} \end{pmatrix} = \begin{pmatrix} -\mu_H^2 + 3\lambda_H h^2 + \lambda_{HS} s^2 & 2\lambda_{HS} h s \\ 2\lambda_{HS} h s & -\mu_S^2 + 3\lambda_S s^2 + \lambda_{HS} h^2 \end{pmatrix} \quad (\text{B.1})$$

where μ_H^2 and μ_S^2 are the mass parameters, and λ_H , λ_S and λ_{HS} are the quartic couplings.

At the EW vacuum, which corresponds to $(v, 0)$ at zero temperature (where $s = 0$), the off-diagonal term of the squared-mass matrix vanishes. This results in the physical masses for the Higgs boson and the new singlet particle, which are given by the eigenvalues of the above squared-mass matrix:

$$m_h^2 = m_h^2(v, 0) = 3v^2 \lambda_H - \mu_H^2, \quad (\text{B.2})$$

$$m_S^2 = m_s^2(v, 0) = \lambda_{HS} v^2 - \mu_S^2. \quad (\text{B.3})$$

The field-dependent masses for other particles in the model, including the gauge bosons and fermions, are given by the following expressions:

$$m_{G^0, G^\pm}^2(h, s) = -\mu_H^2 + \lambda_H h^2 + \lambda_{HS} s^2 \quad (\text{B.4})$$

$$m_W^2(h, s) = \frac{1}{4} g^2 h^2 \quad (\text{B.5})$$

$$m_Z^2(h, s) = \frac{1}{4} (g^2 + g'^2) h^2 \quad (\text{B.6})$$

$$m_\gamma^2(h, s) = 0 \quad (\text{B.7})$$

$$m_f^2(h, s) = \frac{1}{2} y_f^2 h^2 \quad (\text{B.8})$$

The SM gauge couplings are defined at the Z -pole mass scale, M_Z , as:

$$g' = \sqrt{4\pi\alpha_e(M_Z)}, \quad g = \alpha_e(M_Z) / \sin \theta_W, \quad (\text{B.9})$$

where the inputs are derived from precision electroweak data [13]: $\alpha_e^{-1}(M_Z) = 127.944$ and $M_Z = 91.1876$ GeV, which yield $\sin^2 \theta_W = 0.234$.

The Yukawa couplings are evaluated at the quark pole masses using the relation

$$y_f = \sqrt{2} m_f / v, \quad (\text{B.10})$$

where m_f is the measured quark mass. For example, the top quark mass is 172.5 GeV [113].

C Thermal corrections to the mass

Thermal corrections to the mass of particles arise due to the interactions between particles and the thermal bath at finite temperatures. At high temperatures, these interactions modify the effective masses of particles, which can influence the PTs of the system. In the context of this model, these corrections are primarily due to the thermal distribution of particles, which can significantly affect the system's behavior.

The thermal self-energy corrections to the propagators for the fields are represented by the following matrix:

$$\Pi_{h,s} = \begin{pmatrix} \Pi_{hh} & \Pi_{hs} \\ \Pi_{hs} & \Pi_{ss} \end{pmatrix} \quad (\text{C.1})$$

where the individual components are given by:

$$\Pi_{hh} = \left(\frac{3}{16}g^2 + \frac{1}{16}g'^2 + \frac{1}{2}\lambda_H + \frac{1}{4}y_t^2 + \frac{1}{12}\lambda_{HS} \right) T^2 \quad (\text{C.2})$$

$$\Pi_{ss} = \left(\frac{1}{4}\lambda_S + \frac{1}{3}\lambda_{HS} \right) T^2 \quad (\text{C.3})$$

$$\Pi_{hs} \approx 0 \quad (\text{C.4})$$

$$\Pi_{G^0, G^\pm} = \left(\frac{3}{16}g^2 + \frac{1}{16}g'^2 + \frac{1}{2}\lambda_H + \frac{1}{4}y_t^2 + \frac{1}{12}\lambda_{HS} \right) T^2 \quad (\text{C.5})$$

For the longitudinally polarized W^\pm boson, the mass correction due to thermal effects is given by:

$$M_{W_L^\pm}^2 = \frac{1}{4}g^2 h^2 + \frac{11}{6}g^2 T^2 \quad (\text{C.6})$$

The masses of the longitudinal Z boson and the photon (γ_L) are determined by diagonalizing the matrix that includes both the zero-temperature mass term and the thermal corrections:

$$\frac{1}{4}h^2 \begin{pmatrix} g^2 & -gg' \\ -gg' & g'^2 \end{pmatrix} + \begin{pmatrix} \frac{11}{6}g^2 T^2 & 0 \\ 0 & \frac{11}{6}g'^2 T^2 \end{pmatrix} \quad (\text{C.7})$$

The eigenvalues of this matrix give the masses of the longitudinally polarized Z boson and photon. They are:

$$M_{Z_L, \gamma_L}^2 = \frac{1}{8}(g^2 + g'^2)h^2 + \frac{11}{12}(g^2 + g'^2)T^2 \pm \frac{1}{24}\Delta \quad (\text{C.8})$$

where

$$\Delta^2 = -176g^2 g'^2 T^2 (3h^2 + 11T^2) + (g^2 + g'^2)^2 (3h^2 + 22T^2)^2 \quad (\text{C.9})$$

The thermal corrections to the masses of the W^\pm , Z and photon fields are crucial for determining the behavior of the electroweak sector at high temperatures. These corrections shift the masses of the longitudinal components of the gauge bosons and alter the vacuum structure and EWPT patterns in the system. The key dependence on temperature comes from the thermal self-energy contributions, which introduce a temperature-dependent mass term that modifies the dynamics of the system, particularly near the critical temperature for electroweak symmetry breaking.

D Renormalization group equations

RGEs describe the evolution of parameters (such as coupling constants) of a quantum field theory with respect to changes in the energy scale μ . The one-loop RGEs for the quartic couplings λ_H , λ_{HS} and λ_S , along with the gauge and Yukawa couplings, are given by the following set of equations [20]:

$$\begin{aligned} 16\pi^2 \frac{d\lambda_H}{dt} &= \frac{3}{8}g'^4 + \frac{9}{8}g^4 + \frac{3}{4}g'^2 g^2 - 6y_t^4 + 24\lambda_H^2 + 12y_t^2 \lambda_H - 3g'^2 \lambda_H - 9g^2 \lambda_H + \frac{1}{2}\lambda_{HS}^2 \\ 16\pi^2 \frac{d\lambda_{HS}}{dt} &= \lambda_{HS} \left(12\lambda_H + 6\lambda_S + 4\lambda_{HS} + 6y_t^2 - \frac{3}{2}g'^2 - \frac{9}{2}g^2 \right) \\ 16\pi^2 \frac{d\lambda_S}{dt} &= 2\lambda_{HS}^2 + 18\lambda_S^2 \\ 16\pi^2 \frac{dg'}{dt} &= \frac{41}{6}g'^3 \\ 16\pi^2 \frac{dg}{dt} &= -\frac{19}{6}g^3 \\ 16\pi^2 \frac{dg_s}{dt} &= -7g_s^3 \\ 16\pi^2 \frac{dy_t}{dt} &= y_t \left(\frac{9}{2}y_t^2 - \frac{17}{12}g'^2 - \frac{9}{4}g^2 - 8g_s^2 \right) \end{aligned} \quad (\text{D.1})$$

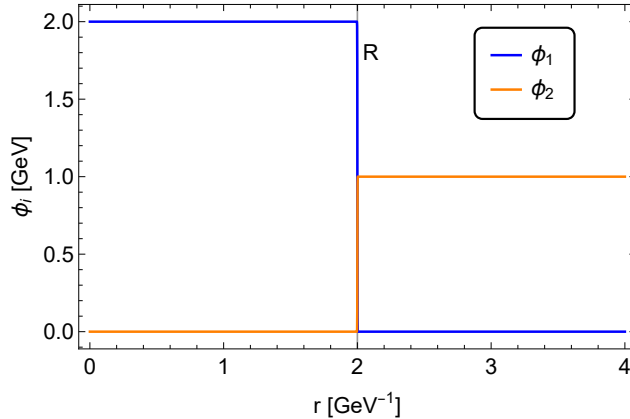


Figure 22: A schematic example of the field configuration for a thin-wall bubble consisting of two fields, ϕ_1 and ϕ_2 is presented. This example illustrates the spatial variation of the field values across the bubble wall, highlighting the sharp transition between the interior and exterior regions of the bubble.

Here, $t \equiv \ln(\mu/m_z)$ represents the running scale, with μ being the renormalization scale.

In our analysis these couplings are input at the Z -pole mass M_Z . In addition to two free parameters λ_{HS} and λ_S , the remaining parameters are fixed based on experimental values. These include: the Higgs quartic coupling $\lambda_H = 0.129$, the strong coupling $g_s = \sqrt{4\pi \times \alpha_s(M_Z)}$, where $\alpha_s(M_Z) = 0.1180$ [13], and other couplings as specified in (B.9) and (B.10).

To determine the energy scale of the Landau pole, we examine the coupling parameters λ_{HS} and λ_S . We then identify the energy scales at which these parameters diverge, taking the numerical divergence to be at 4π . These energy scales are illustrated in Fig. 1. To understand the behavior of the theory at high energy scales, particularly the existence of a Landau pole, we examine the evolution of the coupling constants λ_{HS} and λ_S . The Landau pole occurs when a coupling diverges at some high energy scale. The point at which this divergence occurs can be numerically estimated by identifying the energy scale μ at which the coupling reaches a critical value, typically 4π . The result is illustrated in Fig. 1. This is often referred to as the energy scale where the theory becomes non-perturbative, and it is no longer valid to describe the interactions with a simple perturbative expansion.

E Surface energy density of thin-wall bubbles

For a bubble described by the field configuration $\vec{\phi} = (\phi_1, \phi_2, \dots)$, the free energy (relative to that of the false vacuum phase) is

$$F[\vec{\phi}] = \int_0^\infty dr \, 4\pi r^2 \left[\sum_i \frac{1}{2} \left(\frac{d\phi_i(r)}{dr} \right)^2 + \tilde{V}(\vec{\phi}(r)) \right] \quad (\text{E.1})$$

where $\tilde{V}(\vec{\phi}) \equiv V_{\text{eff}}(\vec{\phi}) - V_{\text{eff}}(\vec{\phi}_F)$.

In general, finding an analytic solution to the bubble profile $\vec{\phi}$ is not possible. However, in the case of thin-wall bubbles, where the wall thickness is much smaller than the bubble radius, $L_w \ll R_b$ (an example of the two-field bubble profile is given in Fig. 22), the calculation can be simplified by dividing the integral into three distinct regions: (i) inside the bubble $r < r_+ \equiv R_b - L_w/2$, (ii) outside the bubble $r > r_- \equiv R_b + L_w/2$ and (iii) inside the wall $r_+ \leq r \leq r_-$. Inside the bubble, the field ϕ approaches its true vacuum value, ϕ_T and $\tilde{V}(\phi) = -\Delta V$, where $\Delta V = V_{\text{eff}}(\vec{\phi}_F) - V_{\text{eff}}(\vec{\phi}_T)$.

Outside the bubble, the field approaches the false vacuum ϕ_F , and $\tilde{V}(\phi) = 0$. In both of these regions, $d\phi_i/dr$ is negligibly small and can be neglected, so the contribution from the integral outside the bubble is effectively zero. On the other hand, since the wall thickness L_w is assumed to be very small, the factor $4\pi r^2$ inside the wall changes so slowly that can be approximated as a constant, $4\pi R_b^2$. Thus, the free energy becomes

$$F[\vec{\phi}] = \int_0^{r_+} dr 4\pi r^2 (-\Delta V) + 4\pi R_b^2 \int_{r_+}^{r_-} dr \left[\sum_i \frac{1}{2} \left(\frac{d\phi_i}{dr} \right)^2 + \tilde{V}(\vec{\phi}) \right] \quad (\text{E.2})$$

$$\simeq -\frac{4}{3}\pi R_b^3 \Delta V + 4\pi R_b^2 \sigma \quad (\text{E.3})$$

where σ is the surface energy density of the bubble wall, defined as the energy stored per unit area of the wall surface:

$$\sigma = \int_{r_+}^{r_-} dr \left[\sum_i \frac{1}{2} \left(\frac{d\phi_i}{dr} \right)^2 + \tilde{V}(\vec{\phi}) \right] \quad (\text{E.4})$$

The two terms in the integral are related to each other through the equation of motion for the extremum of the functional, as described in Eq. (22), which the field configuration obeys.

$$\frac{d^2 \phi_i}{dr^2} = \frac{\partial \tilde{V}(\vec{\phi})}{\partial \phi_i} \quad (\text{E.5})$$

Compared with Eq. (5.1), the friction term proportional to r^{-1} is absent for any field configuration inside the wall. While the form of the equations is relatively simple, it is not possible to solve for an individual ϕ_i , unlike the single-field case. However, there is a differential relationship among all the fields that make up the bubbles.

$$\sum_i \frac{1}{2} \left(\frac{d\phi_i}{dr} \right)^2 = \tilde{V}(\vec{\phi}) \quad (\text{E.6})$$

Given this relation, the surface energy density σ in the general case becomes:

$$\sigma = \int_{r_+}^{r_-} dr \sum_i \left(\frac{d\phi_i}{dr} \right)^2 = \int_0^\infty dr \sum_i \left(\frac{d\phi_i}{dr} \right)^2 \quad (\text{E.7})$$

Note that the integral range has been formally extended from the bubble center to the infinity.

F Modes of bubble nucleation

Depending on the order of expansion, three distinct analytical approximations for $S_E(t)$ typically emerge, each corresponding to a different nucleation mode [99]. In Fig. 23 we illustrate the curves of S_E for these various nucleation modes.

(i) *Constant nucleation.* In this scenario, all higher-order terms in the expansion of S_E are negligible except for the zeroth-order term. This results in:

$$S_E(t) = S_E(t_*) + R_0(t_*; t) \quad (\text{F.1})$$

where $R_0(t_*; t)$ is the zeroth-order remainder term, given in the Lagrange form by:

$$R_0(t_*; t) = \left. \frac{dS_E(t)}{dt} \right|_{t_\xi} (t - t_*) = -\beta_\xi (t - t_*) \quad (\text{F.2})$$

Here, $t_* < t_\xi < t$ and $\beta_\xi \equiv \beta(T_\xi)$.

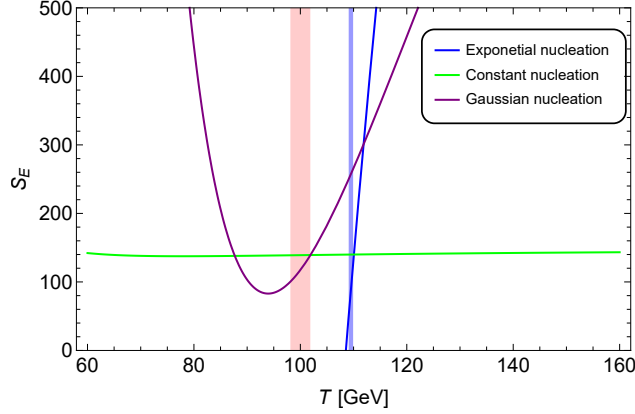


Figure 23: The typical curves of S_E for various nucleation modes are illustrated. The blue shaded region indicates the temperature range where exponential nucleation occurs, while the pink shaded region highlights the temperature range within which other modes of bubble nucleation takes place.

Assuming that the PT occurs during the radiation-dominated (RD) period (as is assumed throughout this paper), the time difference $t - t_* = (H^{-1}(T) - H^{-1}(T_*)) / 2$ and $\beta \equiv H(T)T \frac{dS_E(T)}{dT}$ decreases monotonically with decreasing temperature during the PT⁹. Thus, we obtain the following estimate for $|R_0(t_*; t)|$:

$$|R_0(t_*; t)| < \left| \frac{\beta_*}{2} \left(\frac{1}{H} - \frac{1}{H_*} \right) \right| = \frac{1}{2} \left| \frac{\beta_*}{H_*} \left(\frac{T_*^2}{T^2} - 1 \right) \right| \quad (\text{F.3})$$

where the relation $H(T) \sim T^2$ is used for the RD universe.

To ensure the error in this approximation is smaller than a given tolerance ϵ_0 , i.e., $|R_0(t_*; t)| = |S_E(t) - S_E(t_*)| \leq \epsilon_0$, we set $T_* = T_n$ and $T = T_p$. This gives the following condition:

$$\frac{1}{2} \left| \frac{\beta_n}{H_n} \right| \left(\frac{T_n^2}{T_p^2} - 1 \right) \leq \epsilon_0 \quad (\text{F.4})$$

(ii) *Exponential nucleation.* In this case, the tunneling action $S_E(t)$ can be approximated to first order as follows:

$$S_E(t) = S_E(t_*) + \left. \frac{dS_E(t)}{dt} \right|_{t_*} (t - t_*) + R_1(t_*; t) \quad (\text{F.5})$$

where $R_1(t_*; t)$ represents the first-order remainder term, expressed as:

$$R_1(t_*; t) = \left. \frac{1}{2} \frac{d^2 S_E(t)}{dt^2} \right|_{t_\xi} (t - t_*)^2 \quad (\text{F.6})$$

where $t_* < t_\xi < t$. Introducing the additional parameter $\beta'^2(T) = H(T)^2 T^2 \frac{d^2 S_E}{dT^2}$, we can expand this expression:

$$|R_1(t_*; t)| = \frac{1}{2} \left| 3\beta'_\xi H_\xi + \beta'_\xi{}^2 \right| (t - t_*)^2 \quad (\text{F.7})$$

Given a negligible change in $d^2 S_E / dT^2$ during the PT, we can assume that β' decreases monotonically with temperature during the PT. This yields:

$$|R_1(t_*; t)| < \frac{1}{8} \left| \frac{3\beta_*}{H_*} + \frac{\beta_*'^2}{H_*^2} \right| \left(\frac{T_*^2}{T^2} - 1 \right)^2. \quad (\text{F.8})$$

⁹Here, we focus on fast PTs where the assumption $T_n > T_p > T_m$, with T_m being the temperature at which $S_E(T)$ extremizes and $\beta_m \equiv \beta(T_m) = 0$ is reasonable. For slow PTs (e.g., supercooled PTs), scenarios where $T_p < T_n \sim T_m$ may arise, and the assumption of radiation dominance may break down. We exclude this scenario from our discussion.

To ensure that the error in this approximation remains bounded by ϵ_1 during the PT, specifically that $|R_1(t_*; t)| \leq \epsilon_1$, we set $T_* = T_n$ and $T = T_p$. This leads to the following condition:

$$\frac{1}{8} \left| \frac{3\beta_n}{H_n} + \frac{\beta_n'^2}{H_n^2} \right| \left(\frac{T_n^2}{T_p^2} - 1 \right)^2 \leq \epsilon_1 \quad (\text{F.9})$$

In addition, to distinguish this nucleation mode from constant nucleation, we impose the following condition:

$$\epsilon_0 < \frac{1}{2} \left| \frac{\beta_p}{H_p} \right| \left(1 - \frac{T_p^2}{T_n^2} \right) < |R_0(t_*; t)| \quad (\text{F.10})$$

This criterion confirms the validity of the exponential nucleation approximation and differentiates it from constant nucleation. Exponential nucleation typically arises in the regime where the tunneling action is largely influenced by an exponentially suppressed rate, as depicted by the blue curve in Fig. 23.

(iii) *Gaussian (Simultaneous) nucleation.* In the case of Gaussian (simultaneous) nucleation, when t_* is selected at the extremum of $S_E(t)$, denoted as t_m , the first-order derivative of $S_E(t)$ becomes zero. Thus, $S_E(t)$ can be approximated to second order as follows:

$$S(t) = S(t_m) + \frac{1}{2} \frac{d^2 S(t)}{dt^2} \Big|_{t_m} (t - t_m)^2 + R_2(t_m; t) \quad (\text{F.11})$$

where $R_2(t_m; t)$ is the second-order remainder term, expressed as:

$$R_2(t_m; t) = \frac{1}{3!} \frac{d^3 S(t)}{dt^3} \Big|_{t_\xi} (t - t_m)^3 \quad (\text{F.12})$$

where $t < t_\xi < t_m$. In terms of β and β' parameters, it can be written as:

$$|R_2(t_m; t)| = \frac{1}{6} \left| 15\beta_\xi H_\xi^2 + 9\beta_\xi'^2 H_\xi + \beta_\xi''^3 \right| (t_m - t)^3 \quad (\text{F.13})$$

where $\beta''^3(T) = H(T)^3 T^3 \frac{d^3 S_E}{dT^3}$. For the case where $\beta'' > 0$ during the PT within temperature range from T_n to T_p , we have

$$|R_2(t_m; t)| < \frac{1}{48} \left| \left(\frac{15\beta}{H} + \frac{9\beta'^2}{H^2} \right) \right| \left(\frac{T^2}{T_m^2} - 1 \right)^3 \quad (\text{F.14})$$

To ensure that the error in this approximation is bounded by ϵ_2 during the PT from T_n to T_p , specifically, that $|R_2(t_m; t)| \leq \epsilon_2$, we set $T = T_n$. Therefore, the following condition must be satisfied:

$$\frac{1}{16} \left| \left(\frac{5\beta_n}{H_n} + \frac{3\beta_n'^2}{H_n^2} \right) \right| \left(\frac{T_n^2}{T_m^2} - 1 \right)^3 \leq \epsilon_2 \quad (\text{F.15})$$

On the other hand, note that $R_0(t_m; t) = R_1(t_m; t)$ in this case. To distinguish this from constant nucleation, one should impose the condition $|R_0(t_m; t_n)| > \epsilon_0$, which is satisfied provided that

$$|R_0(t_m; t_n)| = \frac{1}{8} \frac{\beta_m'^2}{H_m^2} \left(1 - \frac{T_m^2}{T_n^2} \right)^2 > \epsilon_0. \quad (\text{F.16})$$

References

- [1] V.A. Kuzmin, V.A. Rubakov and M.E. Shaposhnikov, On the Anomalous Electroweak Baryon Number Nonconservation in the Early Universe, [Phys. Lett. B](#) **155** (1985) 36.

- [2] A.G. Cohen, D.B. Kaplan and A.E. Nelson, Progress in electroweak baryogenesis, [Ann. Rev. Nucl. Part. Sci.](#) **43** (1993) 27 [[hep-ph/9302210](#)].
- [3] V.A. Rubakov and M.E. Shaposhnikov, Electroweak baryon number nonconservation in the early universe and in high-energy collisions, [Usp. Fiz. Nauk](#) **166** (1996) 493 [[hep-ph/9603208](#)].
- [4] D.E. Morrissey and M.J. Ramsey-Musolf, Electroweak baryogenesis, [New J. Phys.](#) **14** (2012) 125003 [[1206.2942](#)].
- [5] V. Kuzmin, V. Rubakov and M. Shaposhnikov, On anomalous electroweak baryon-number non-conservation in the early universe, [Physics Letters B](#) **155** (1985) 36.
- [6] A. Kosowsky, M.S. Turner and R. Watkins, Gravitational waves from first order cosmological phase transitions, [Phys. Rev. Lett.](#) **69** (1992) 2026.
- [7] C. Caprini et al., Science with the space-based interferometer eLISA. II: Gravitational waves from cosmological phase transitions, [JCAP](#) **04** (2016) 001 [[1512.06239](#)].
- [8] Z.-C. Liang, Y.-M. Hu, Y. Jiang, J. Cheng, J.-d. Zhang and J. Mei, Science with the TianQin Observatory: Preliminary results on stochastic gravitational-wave background, [Phys. Rev. D](#) **105** (2022) 022001 [[2107.08643](#)].
- [9] C. Caprini et al., Detecting gravitational waves from cosmological phase transitions with LISA: an update, [JCAP](#) **03** (2020) 024 [[1910.13125](#)].
- [10] W.-H. Ruan, Z.-K. Guo, R.-G. Cai and Y.-Z. Zhang, Taiji program: Gravitational-wave sources, [Int. J. Mod. Phys. A](#) **35** (2020) 2050075 [[1807.09495](#)].
- [11] K. Kajantie, M. Laine, K. Rummukainen and M.E. Shaposhnikov, The Electroweak phase transition: A Nonperturbative analysis, [Nucl. Phys. B](#) **466** (1996) 189 [[hep-lat/9510020](#)].
- [12] F. Csikor, Z. Fodor and J. Heitger, End point of the hot electroweak phase transition, [Phys. Rev. Lett.](#) **82** (1999) 21.
- [13] PARTICLE DATA GROUP COLLABORATION collaboration, Review of particle physics, [Phys. Rev. D](#) **110** (2024) 030001.
- [14] M. D’Onofrio, K. Rummukainen and A. Tranberg, Sphaleron Rate in the Minimal Standard Model, [Phys. Rev. Lett.](#) **113** (2014) 141602 [[1404.3565](#)].
- [15] M. D’Onofrio and K. Rummukainen, Standard model cross-over on the lattice, [Phys. Rev. D](#) **93** (2016) 025003 [[1508.07161](#)].
- [16] S. Profumo, M.J. Ramsey-Musolf and G. Shaughnessy, Singlet Higgs phenomenology and the electroweak phase transition, [JHEP](#) **08** (2007) 010 [[0705.2425](#)].
- [17] A. Ahriche, What is the criterion for a strong first order electroweak phase transition in singlet models?, [Phys. Rev. D](#) **75** (2007) 083522 [[hep-ph/0701192](#)].
- [18] A. Friedlander, I. Banta, J.M. Cline and D. Tucker-Smith, Wall speed and shape in singlet-assisted strong electroweak phase transitions, [Phys. Rev. D](#) **103** (2021) 055020 [[2009.14295](#)].
- [19] J. Ellis, M. Lewicki, M. Merchand, J.M. No and M. Zych, The scalar singlet extension of the Standard Model: gravitational waves versus baryogenesis, [JHEP](#) **01** (2023) 093 [[2210.16305](#)].

- [20] D. Curtin, P. Meade and C.-T. Yu, Testing Electroweak Baryogenesis with Future Colliders, [JHEP](#) **11** (2014) 127 [[1409.0005](#)].
- [21] J.R. Espinosa, T. Konstandin and F. Riva, Strong Electroweak Phase Transitions in the Standard Model with a Singlet, [Nucl. Phys. B](#) **854** (2012) 592 [[1107.5441](#)].
- [22] S. Profumo, M.J. Ramsey-Musolf, C.L. Wainwright and P. Winslow, Singlet-catalyzed electroweak phase transitions and precision Higgs boson studies, [Phys. Rev. D](#) **91** (2015) 035018 [[1407.5342](#)].
- [23] A. Beniwal, M. Lewicki, J.D. Wells, M. White and A.G. Williams, Gravitational wave, collider and dark matter signals from a scalar singlet electroweak baryogenesis, [JHEP](#) **08** (2017) 108 [[1702.06124](#)].
- [24] V. Vaskonen, Electroweak baryogenesis and gravitational waves from a real scalar singlet, [Phys. Rev. D](#) **95** (2017) 123515 [[1611.02073](#)].
- [25] G. Kurup and M. Perelstein, Dynamics of Electroweak Phase Transition In Singlet-Scalar Extension of the Standard Model, [Phys. Rev. D](#) **96** (2017) 015036 [[1704.03381](#)].
- [26] M. Carena, Z. Liu and Y. Wang, Electroweak phase transition with spontaneous Z_2 -breaking, [JHEP](#) **08** (2020) 107 [[1911.10206](#)].
- [27] J.M. Cline and P.-A. Lemieux, Electroweak phase transition in two Higgs doublet models, [Phys. Rev. D](#) **55** (1997) 3873 [[hep-ph/9609240](#)].
- [28] L. Wang, J.M. Yang and Y. Zhang, Two-Higgs-doublet models in light of current experiments: a brief review, [Commun. Theor. Phys.](#) **74** (2022) 097202 [[2203.07244](#)].
- [29] L. Fromme, S.J. Huber and M. Seniuch, Baryogenesis in the two-Higgs doublet model, [JHEP](#) **11** (2006) 038 [[hep-ph/0605242](#)].
- [30] T. Biekötter, S. Heinemeyer, J.M. No, M.O. Olea-Romacho and G. Weiglein, The trap in the early Universe: impact on the interplay between gravitational waves and LHC physics in the 2HDM, [JCAP](#) **03** (2023) 031 [[2208.14466](#)].
- [31] J. Bernon, L. Bian and Y. Jiang, A new insight into the phase transition in the early Universe with two Higgs doublets, [JHEP](#) **05** (2018) 151 [[1712.08430](#)].
- [32] M. Aoki, T. Komatsu and H. Shibuya, Possibility of a multi-step electroweak phase transition in the two-Higgs doublet models, [PTEP](#) **2022** (2022) 063B05 [[2106.03439](#)].
- [33] N. Benincasa, L. Delle, K. Kannike and L. Marzola, Multi-steps phase transitions and gravitational waves in the inert doublet model, [Frascati Phys. Ser.](#) **72** (2022) 9.
- [34] J.M. Cline and G.D. Moore, Supersymmetric electroweak phase transition: Baryogenesis versus experimental constraints, [Phys. Rev. Lett.](#) **81** (1998) 3315 [[hep-ph/9806354](#)].
- [35] K. Funakubo, S. Tao and F. Toyoda, Phase transitions in the NMSSM, [Prog. Theor. Phys.](#) **114** (2005) 369 [[hep-ph/0501052](#)].
- [36] S.J. Huber, T. Konstandin, T. Prokopec and M.G. Schmidt, Electroweak Phase Transition and Baryogenesis in the nMSSM, [Nucl. Phys. B](#) **757** (2006) 172 [[hep-ph/0606298](#)].

- [37] S. Baum, M. Carena, N.R. Shah, C.E.M. Wagner and Y. Wang, Nucleation is more than critical: A case study of the electroweak phase transition in the NMSSM, [JHEP **03** \(2021\) 055](#) [[2009.10743](#)].
- [38] T. Biekötter, S. Heinemeyer, J.M. No, M.O. Olea and G. Weiglein, Fate of electroweak symmetry in the early Universe: Non-restoration and trapped vacua in the N2HDM, [JCAP **06** \(2021\) 018](#) [[2103.12707](#)].
- [39] C. Grojean, G. Servant and J.D. Wells, First-order electroweak phase transition in the standard model with a low cutoff, [Phys. Rev. D **71** \(2005\) 036001](#) [[hep-ph/0407019](#)].
- [40] C. Delaunay, C. Grojean and J.D. Wells, Dynamics of Non-renormalizable Electroweak Symmetry Breaking, [JHEP **04** \(2008\) 029](#) [[0711.2511](#)].
- [41] M. Chala, C. Krause and G. Nardini, Signals of the electroweak phase transition at colliders and gravitational wave observatories, [JHEP **07** \(2018\) 062](#) [[1802.02168](#)].
- [42] J. Ellis, M. Lewicki and J.M. No, On the Maximal Strength of a First-Order Electroweak Phase Transition and its Gravitational Wave Signal, [JCAP **04** \(2019\) 003](#) [[1809.08242](#)].
- [43] R.-G. Cai, M. Sasaki and S.-J. Wang, The gravitational waves from the first-order phase transition with a dimension-six operator, [JCAP **08** \(2017\) 004](#) [[1707.03001](#)].
- [44] R.-G. Cai, K. Hashino, S.-J. Wang and J.-H. Yu, Gravitational waves from patterns of electroweak symmetry breaking: an effective perspective, [2202.08295](#).
- [45] R. Jinno and M. Takimoto, Gravitational waves from bubble collisions: An analytic derivation, [Phys. Rev. D **95** \(2017\) 024009](#) [[1605.01403](#)].
- [46] R. Jinno and M. Takimoto, Gravitational waves from bubble dynamics: Beyond the Envelope, [JCAP **01** \(2019\) 060](#) [[1707.03111](#)].
- [47] J. Kozaczuk, M.J. Ramsey-Musolf and J. Shelton, Exotic Higgs boson decays and the electroweak phase transition, [Phys. Rev. D **101** \(2020\) 115035](#) [[1911.10210](#)].
- [48] A.H. Guth and E.J. Weinberg, Could the Universe Have Recovered from a Slow First Order Phase Transition?, [Nucl. Phys. B **212** \(1983\) 321](#).
- [49] A.H. Guth, Eternal inflation and its implications, [J. Phys. A **40** \(2007\) 6811](#) [[hep-th/0702178](#)].
- [50] J.R. Espinosa, M. Losada and A. Riotto, Symmetry nonrestoration at high temperature in little Higgs models, [Phys. Rev. D **72** \(2005\) 043520](#) [[hep-ph/0409070](#)].
- [51] I. Baldes and G. Servant, High scale electroweak phase transition: baryogenesis & symmetry non-restoration, [JHEP **10** \(2018\) 053](#) [[1807.08770](#)].
- [52] P. Meade and H. Ramani, Unrestored Electroweak Symmetry, [Phys. Rev. Lett. **122** \(2019\) 041802](#) [[1807.07578](#)].
- [53] O. Matsedonskyi and G. Servant, High-Temperature Electroweak Symmetry Non-Restoration from New Fermions and Implications for Baryogenesis, [JHEP **09** \(2020\) 012](#) [[2002.05174](#)].

- [54] A. Angelescu, F. Goertz and A. Tada, [Z₂ non-restoration and composite Higgs: singlet-assisted baryogenesis w/o topological defects](#), [JHEP](#) **10** (2022) 019 [[2112.12087](#)].
- [55] A. Angelescu and P. Huang, [Multistep Strongly First Order Phase Transitions from New Fermions at the TeV Scale](#), [Phys. Rev. D](#) **99** (2019) 055023 [[1812.08293](#)].
- [56] Q.-H. Cao, K. Hashino, X.-X. Li and J.-H. Yue, [Multi-step phase transition and gravitational wave from general Z₂ scalar extensions](#), [2212.07756](#).
- [57] A.P. Morais and R. Pasechnik, [Probing multi-step electroweak phase transition with multi-peaked primordial gravitational waves spectra](#), [JCAP](#) **04** (2020) 036 [[1910.00717](#)].
- [58] R. Pasechnik, A.P. Morais and T. Vieu, [Multi-peaked signatures of primordial gravitational waves from multi-step electroweak phase transition](#), in [The Fifteenth Marcel Grossmann Meeting, 2022](#), DOI.
- [59] A. Aguirre, M.C. Johnson and A. Shomer, [Towards observable signatures of other bubble universes](#), [Phys. Rev. D](#) **76** (2007) 063509 [[0704.3473](#)].
- [60] A.P. Morais, R. Pasechnik and T. Vieu, [Multi-peaked signatures of primordial gravitational waves from multi-step electroweak phase transition](#), [PoS EPS-HEP2019](#) (2020) 054 [[1802.10109](#)].
- [61] D. Croon and G. White, [Exotic Gravitational Wave Signatures from Simultaneous Phase Transitions](#), [JHEP](#) **05** (2018) 210 [[1803.05438](#)].
- [62] S. Blasi and A. Mariotti, [Domain Walls Seeding the Electroweak Phase Transition](#), [Phys. Rev. Lett.](#) **129** (2022) 261303 [[2203.16450](#)].
- [63] P. Agrawal, S. Blasi, A. Mariotti and M. Nee, [Electroweak phase transition with a double well done doubly well](#), [JHEP](#) **06** (2024) 089 [[2312.06749](#)].
- [64] U.A. Yajnik, [PHASE TRANSITION INDUCED BY COSMIC STRINGS](#), [Phys. Rev. D](#) **34** (1986) 1237.
- [65] I. Dasgupta, [Vacuum tunneling by cosmic strings](#), [Nucl. Phys. B](#) **506** (1997) 421 [[hep-th/9702041](#)].
- [66] P.J. Steinhardt, [Monopole and Vortex Dissociation and Decay of the False Vacuum](#), [Nucl. Phys. B](#) **190** (1981) 583.
- [67] B. Kumar, M.B. Paranjape and U.A. Yajnik, [Fate of the false monopoles: Induced vacuum decay](#), [Phys. Rev. D](#) **82** (2010) 025022 [[1006.0693](#)].
- [68] P. Agrawal and M. Nee, [The Boring Monopole](#), [SciPost Phys.](#) **13** (2022) 049 [[2202.11102](#)].
- [69] D. Wei, H. Chen, Q. Fan and Y. Jiang, [Cosmological first-order phase transitions without bubbles](#), [2401.08801](#).
- [70] W.-L. Guo and Y.-L. Wu, [The Real singlet scalar dark matter model](#), [JHEP](#) **10** (2010) 083 [[1006.2518](#)].
- [71] J.M. Cline and K. Kainulainen, [Electroweak baryogenesis and dark matter from a singlet Higgs](#), [JCAP](#) **01** (2013) 012 [[1210.4196](#)].
- [72] ATLAS collaboration, [Observation of a new particle in the search for the Standard Model Higgs boson with the ATLAS detector at the LHC](#), [Phys. Lett. B](#) **716** (2012) 1 [[1207.7214](#)].

- [73] CMS collaboration, Observation of a New Boson at a Mass of 125 GeV with the CMS Experiment at the LHC, [Phys. Lett. B](#) **716** (2012) 30 [[1207.7235](#)].
- [74] L. Dolan and R. Jackiw, [Symmetry Behavior at Finite Temperature](#), [Phys. Rev. D](#) **9** (1974) 3320.
- [75] R.R. Parwani, Resummation in a hot scalar field theory, [Phys. Rev. D](#) **45** (1992) 4695 [[hep-ph/9204216](#)].
- [76] P.B. Arnold and O. Espinosa, [The Effective potential and first order phase transitions: Beyond leading-order](#), [Phys. Rev. D](#) **47** (1993) 3546 [[hep-ph/9212235](#)].
- [77] S. Weinberg, [Gauge and Global Symmetries at High Temperature](#), [Phys. Rev. D](#) **9** (1974) 3357.
- [78] M. Carena, C. Krause, Z. Liu and Y. Wang, [New approach to electroweak symmetry nonrestoration](#), [Phys. Rev. D](#) **104** (2021) 055016 [[2104.00638](#)].
- [79] P. Athron, C. Balázs, A. Fowlie and Y. Zhang, [PhaseTracer: tracing cosmological phases and calculating transition properties](#), [Eur. Phys. J. C](#) **80** (2020) 567 [[2003.02859](#)].
- [80] P. Athron, C. Balazs, A. Fowlie, L. Morris, G. White and Y. Zhang, [How arbitrary are perturbative calculations of the electroweak phase transition?](#), [JHEP](#) **01** (2023) 050 [[2208.01319](#)].
- [81] A.D. Linde, Decay of the False Vacuum at Finite Temperature, [Nucl. Phys. B](#) **216** (1983) 421.
- [82] A.D. Linde, Fate of the False Vacuum at Finite Temperature: Theory and Applications, [Phys. Lett. B](#) **100** (1981) 37.
- [83] P. Athron, C. Balázs and L. Morris, [Supercool subtleties of cosmological phase transitions](#), [JCAP](#) **03** (2023) 006 [[2212.07559](#)].
- [84] R. Sato, [SimpleBounce : a simple package for the false vacuum decay](#), [Comput. Phys. Commun.](#) **258** (2021) 107566 [[1908.10868](#)].
- [85] J.R. Espinosa, [A Fresh Look at the Calculation of Tunneling Actions](#), [JCAP](#) **07** (2018) 036 [[1805.03680](#)].
- [86] M.D. Rintoul and S. Torquato, [Precise determination of the critical threshold and exponents in a three-dimensional continuum percolation model](#), [J. Phys. A](#) **30** (1997) L585.
- [87] C.D. Lorenz and R.M. Ziff, [Precise determination of the critical percolation threshold for the three-dimensional “swiss cheese” model using a growth algorithm](#), [The Journal of Chemical Physics](#) **114** (2001) 3659.
- [88] J. Lin and H. Chen, [Continuum percolation of porous media via random packing of overlapping cube-like particles](#), [Theoretical and Applied Mechanics Letters](#) **8** (2018) 299.
- [89] M. Li, H. Chen and J. Lin, [Numerical study for the percolation threshold and transport properties of porous composites comprising non-centrosymmetrical superovoidal pores](#), [Computer Methods in Applied Mechanics and Engineering](#) **361** (2020) 112815.
- [90] A.H. Guth and E.J. Weinberg, [Cosmological Consequences of a First Order Phase Transition in the SU\(5\) Grand Unified Model](#), [Phys. Rev. D](#) **23** (1981) 876.
- [91] M.S. Turner, E.J. Weinberg and L.M. Widrow, [Bubble nucleation in first order inflation and other cosmological phase transitions](#), [Phys. Rev. D](#) **46** (1992) 2384.

- [92] M. Lewicki, M. Merchand and M. Zych, Electroweak bubble wall expansion: gravitational waves and baryogenesis in Standard Model-like thermal plasma, [JHEP **02** \(2022\) 017 \[2111.02393\]](#).
- [93] P. Athron, C. Balázs, A. Fowlie, L. Morris and L. Wu, Cosmological phase transitions: From perturbative particle physics to gravitational waves, [Prog. Part. Nucl. Phys. **135** \(2024\) 104094 \[2305.02357\]](#).
- [94] D. Cutting, E.G. Escartin, M. Hindmarsh and D.J. Weir, Gravitational waves from vacuum first order phase transitions II: from thin to thick walls, [Phys. Rev. D **103** \(2021\) 023531 \[2005.13537\]](#).
- [95] E.W. Kolb, The Early Universe, vol. 69, Taylor and Francis (5, 2019), [10.1201/9780429492860](#).
- [96] J.M. Cline, K. Kainulainen and D. Tucker-Smith, Electroweak baryogenesis from a dark sector, [Phys. Rev. D **95** \(2017\) 115006 \[1702.08909\]](#).
- [97] J.M. Cline, A. Friedlander, D.-M. He, K. Kainulainen, B. Laurent and D. Tucker-Smith, Baryogenesis and gravity waves from a UV-completed electroweak phase transition, [Phys. Rev. D **103** \(2021\) 123529 \[2102.12490\]](#).
- [98] S.R. Coleman, The Fate of the False Vacuum. 1. Semiclassical Theory, [Phys. Rev. D **15** \(1977\) 2929](#).
- [99] A. Megevand and S. Ramirez, Bubble nucleation and growth in very strong cosmological phase transitions, [Nucl. Phys. B **919** \(2017\) 74 \[1611.05853\]](#).
- [100] LISA COSMOLOGY WORKING GROUP collaboration, Cosmology with the Laser Interferometer Space Antenna, [Living Rev. Rel. **26** \(2023\) 5 \[2204.05434\]](#).
- [101] J.M. Cline, K. Kainulainen, P. Scott and C. Weniger, Update on scalar singlet dark matter, [Phys. Rev. D **88** \(2013\) 055025 \[1306.4710\]](#).
- [102] GAMBIT collaboration, Status of the scalar singlet dark matter model, [Eur. Phys. J. C **77** \(2017\) 568 \[1705.07931\]](#).
- [103] T. Alanne, T. Hugle, M. Platscher and K. Schmitz, Low-scale leptogenesis assisted by a real scalar singlet, [JCAP **03** \(2019\) 037 \[1812.04421\]](#).
- [104] M. Le Dall and A. Ritz, Leptogenesis and the Higgs Portal, [Phys. Rev. D **90** \(2014\) 096002 \[1408.2498\]](#).
- [105] T.W.B. Kibble, Topology of Cosmic Domains and Strings, [J. Phys. A **9** \(1976\) 1387](#).
- [106] A. Vilenkin and E. Shellard, Cosmic Strings and Other Topological Defects, Cambridge University Press (1994).
- [107] T. Vachaspati, Kinks and Domain Walls : An Introduction to Classical and Quantum Solitons, Oxford University Press (2007), [10.1017/9781009290456](#).
- [108] R.H. Brandenberger, A.-C. Davis, T. Prokopec and M. Trodden, Local and nonlocal defect mediated electroweak baryogenesis, [Phys. Rev. D **53** \(1996\) 4257 \[hep-ph/9409281\]](#).
- [109] T. Schröder and R. Brandenberger, Embedded domain walls and electroweak baryogenesis, [Phys. Rev. D **110** \(2024\) 043516 \[2404.13035\]](#).
- [110] J. Azzola, O. Matsedonskyi and A. Weiler, Minimal Electroweak Baryogenesis via Domain Walls, [2412.10495](#).
- [111] A. Mariotti, X. Nagels, A. Rase and M. Vanvlasselaer, DW-genesis: baryon number from domain wall network collapse, [2411.13494](#).

- [112] S.R. Coleman and E.J. Weinberg, Radiative Corrections as the Origin of Spontaneous Symmetry Breaking, [Phys. Rev. D](#) **7** (1973) 1888.
- [113] CMS COLLABORATION† AND ATLAS COLLABORATION‡ collaboration, Combination of measurements of the top quark mass from data collected by the atlas and cms experiments at $\sqrt{s} = 7$ and 8 tev, [Phys. Rev. Lett.](#) **132** (2024) 261902.